NTNU

**Norwegian University of
Science and Technology**

Study of Hydrofoil Wakes Using PIV and CFD

Bjarte Grytli Seim

Norwegian University of Science and Technology
Department of Energy and Process Engineering

Problem Description

The objectives of this project are to obtain robust analysis schemes for existing PIV data sets from wake measurements, to be familiar with existing PIV equipment and use CFD for discussing the various results obtained in the experiments. If time and/or overall project progress allows; the use of a new variation of wake manipulating technologies will be included in the thesis project.

Actual PIV work will be made at St. Anthony Falls Laboratory/University of Minnesota during a stay of roughly 4 weeks.

Assignment given: 26. January 2009
Supervisor: Morten Kjeldsen, EPT

Norges teknisk-
naturvitenskapelige universitet
NTNU

Fakultet for ingeniørvitenskap og teknologi
Institutt for energi- og prosessteknikk

EPT-H-2009-61

MASTEROPPGAVE

for

Stud. Tech. Bjarte Grytli Seim
Våren 2009

Study of hydrofoil wakes using PIV and CFD
Studie av vaker nedstrøms hydrofoiler ved hjelp av PIV og CFD

Background

The wakes behind guide vanes in Francis turbines are responsible for increased noise and vibration as well as reduced efficiency of the unit when they interact with the turbine runner. This interaction, and the effects associated with it, is termed rotor stator interaction (RSI). There are considerable incentives for developing designs and technologies that reduce the effects of RSI, the direct gains being increased efficiency and more reliable/less fatigue prone units. The flow field exiting the guide vane cascade consists of a variation due to the pressure differences between adjacent guide-vanes (cascade effect), and a viscous wake from each individual vane. The viscous wake is normally[1] consisting of unsteady structures that are believed to further enhance RSI effects. For years there has been an interest in technologies for manipulating wakes. This technology has mainly been tested in hydrofoil studies where the use of PIV has been important for determining wake flow characteristics. This thesis work is partly motivated by experiences from developing such technology.

Objective

The objectives of this project are to obtain robust analysis schemes for existing PIV data sets from wake measurements, to be familiar with existing PIV equipment and use CFD for discussing the various results obtained in the experiments. If time and/or overall project progress allows; the use of a new variation of wake manipulating technologies will be included in the thesis project.

Actual PIV work will be made at St. Anthony Falls Laboratory/ University of Minnesota during a stay of roughly 4 weeks[2].

The task is approached in the following manner:

1. A literature survey on PIV measurement technology, analysis and wake flows should be given.

---

[1] It should be noted that the guide vane cascade is in an accelerating flow field. The impact of an accelerating flow field on shedding characteristics is yet to be determined.
[2] Prof. Roger E. A. Arndt will act as supervisor in this period.

2. Batch processing of PIV images, for making PIV velocity vector sets, should be done using the software PivTec or LAVision native software.
3. Software should be made, using e.g. LabView, for further post processing of PIV vector sets.
4. CFD analysis shall be made while discussing results from PIV experiments.

---- " ---

Senest 14 dager etter utlevering av oppgaven skal kandidaten levere/sende instituttet en detaljert fremdrift- og evt. forsøksplan for oppgaven til evaluering og evt. diskusjon med faglig ansvarlig/ veiledere. Detaljer ved evt. utførelse av dataprogrammer skal avtales nærmere i samråd med faglig ansvarlig.

Besvarelsen redigeres mest mulig som en forskningsrapport med et sammendrag både på norsk og engelsk, konklusjon, litteraturliste, innholdsfortegnelse etc. Ved utarbeidelsen av teksten skal kandidaten legge vekt på å gjøre teksten oversiktlig og velskrevet. Med henblikk på lesning av besvarelsen er det viktig at de nødvendige henvisninger for korresponderende steder i tekst, tabeller og figurer anføres på begge steder. Ved bedømmelsen legges det stor vekt på at resultatene er grundig bearbeidet, at de oppstilles tabellarisk og/eller grafisk på en oversiktlig måte, og at de er diskutert utførlig.

Alle benyttede kilder, også muntlige opplysninger, skal oppgis på fullstendig måte. (For tidsskrifter og bøker oppgis forfatter, tittel, årgang, sidetall og evt. figurnummer.)

Det forutsettes at kandidaten tar initiativ til og holder nødvendig kontakt med faglærer og veileder(e). Kandidaten skal rette seg etter de reglementer og retningslinjer som gjelder ved alle fagmiljøer som kandidaten har kontakt med gjennom sin utførelse av oppgaven, samt etter eventuelle pålegg fra Institutt for energi- og prosessteknikk.
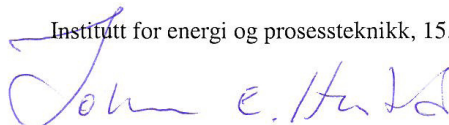
I henhold til "Utfyllende regler til studieforskriften for teknologistudiet/sivilingeniørstudiet" ved NTNU § 20, forbeholder instituttet seg retten til å benytte alle resultater i undervisnings- og forskningsformål, samt til publikasjoner.

Ett -1 komplett eksemplar av originalbesvarelsen av oppgaven skal innleveres til samme adressat som den ble utlevert fra. (Det skal medfølge et konsentrert sammendrag på maks. en maskinskrevet side med dobbel linjeavstand med forfatternavn og oppgavetittel for evt. referering i tidsskrifter).

Til Instituttet innleveres to - 2 komplette, kopier av besvarelsen. Ytterligere kopier til evt. medveiledere/oppgavegivere skal avtales med, og evt. leveres direkte til, de respektive.

Til instituttet innleveres også en komplett kopi (inkl. konsentrerte sammendrag) på CD-ROM i Word-format eller tilsvarende.

Institutt for energi og prosessteknikk, 15. januar 2009

Johan E. Hustad
Instituttleder

Morten Kjeldsen
Faglærer/veileder

Medveiledere/
Co-supervisors: Roger E. A. Arndt, University of Minnesota
                    Torbjørn Nielsen
                    Ingunn Granstrøm, Skagerak Energi

Acknowledgments

Sammendrag

I denne masteroppgava blir vaken til en hydrofoil undersøkt med bruk av PIV. Målet med oppgave har vært å undersøke hvordan vortex generatorer kan jevne ut hastighets forskjellene i hydrofoil vaker. Studiet er motivert av rotor stator interaksjoner i Francis turbiner der ideen er at en jevnere vake fra stator kan minke kreftene på rotor og dermed øke levetida til Francis turbiner.

Et litteratur søk på vake teori har blitt gjennomført. Dette litteratursøket motiverte bruken av en normalisering av hastighetene i vaken.

Det ble gjennomført et ekperimentelt arbeid ved vanntunnelen ved Saint Anthony Falls Laboratory ved University of Minnesota. Der ble det gjort tester på en NACA0015 hydrofoil med fire ulike vortex generator oppsett for et sett med angrepsvinkler og hastigheter.

Lift og drag krefter på hydrofoilen ble målt med en kraftbalanse. På grunn av unøyaktighet i drag målingen kunne den ikke bli brukt til å sammenligne drag mellom de ulike vortex generator oppsettene. Dette førte til at drag ble prøvd undersøkt ved hjelp av hastighets forskjellene i vaken. Hvor riktig denne undersøkelsen har blitt diskutert ved hjelp av CFD. CFD ble også brukt for å få innsikt i hvordan fordelingen av trykk og hastigheter var i vanntunnelen.

PIV bilder fra testene har blitt prosessert til vektorfelt ved bruk av det kommersielle PIV programmet DaVis7. For å analysere vektorfeltene videre har både DaVis7 blitt brukt og egne Matlab programmer.

For kunne sammenligne ulike vakeprofiler med målbare størrelser, ble det undersøkt hvorvidt et standard vake profil kunne brukes. Da det standard vake profilet er symmetrisk kan det kun beskrive målte vaker for angrepsvinkler rundt 0°. Videre viste det seg at bruk av de fleste vortex generatorer førte til vaker som ikke kunne beskrives med det standard vake profilet.

Vortex generatoren som gav best utjevning av vaken for de målepunktene det ble analysert for var en V-formet 1 mm vortex generator. Denne vortex generatoren førte til mindre drag enn noen av de andre vortex generatorene som ble testet. Hydrofoilen uten vortex generatorer ble likevel beregnet til å ha minst drag for de analyserte målepunktene.

Hastighets utjevningen av vaken ved vortexs generatorer har blitt observert til å være såpass god for enkelte målepunter at det kan være av interesse å fortsette studier på hvorvidt vortex generatorer kan øke levetiden på Francis turbiner.

Abstract

In this master thesis the wake of a hydrofoil have been investigated using PIV. The main goal of this work have been to investigate how vortex generators can create mixing and smoothing of the velocity deficit in hydrofoil wakes. This study is motivated by the rotor stator interactions in Francis turbines with the idea that smoother wakes from the stator can reduce the forces on the rotor and hence increase the life span of Francis turbines.

A literature survey of foil theory and wake flows have been carried out. This survey motivated the use of a normalization of the velocity in the wake.

Experimental work was carried out at the water tunnel facility at Saint Anthony Falls Laboratory at the University of Minnesota. Tests were performed on a NACA0015 hydrofoil with four different vortex generator configurations, for a range of different angles of attack and velocities.

Lift and drag forces on the hydrofoil was measured using a force balance. Because the drag measurement had poor accuracy, it could not be used to compare the different vortex generator configurations in terms of drag. As a result the drag was investigated using the velocity deficit in the wakes. The quality of this analysis have been discussed with the use of CFD. CFD is also used to gain insight into how pressure and velocity is distributed in the water tunnel.

The PIV images from the tests have been processed into vector fields with the commercial PIV software DaVis7. For analyzing the PIV data further, different post-processing schemes in DaVis7 was investigated together with programs developed in Matlab.

In order to compare the wakes resulting from the use of different vortex generators with measurable quantities, the use of a standard wake profile has been investigated. The standard wake profile is symmetrical and could hence only describe wake measurements done at an angle of attack close to $0°$. Furthermore it turned out that most vortex generators resulted in a wake that could not be described with the standard wake profile.

The vortex generator configurations that gave the best smoothing of the hydrofoil wake for the investigated operation points turned out to be a $1 \, \text{mm}$ V-shaped vortex generator. This vortex generator also caused less drag than than the other vortex generators tested. However, the use of vortex generators resulted in increased drag compared to the plain hydrofoil for the analyzed operating points.

The velocity deficit in the wake is shown to get so well smoothed out for some tested cases that it is considered worth while to continue the investigation on vortex generators capability to increase the lifespan of Francis turbines.

Contents

List of Figures

List of Tables

Nomenclature

Symbol	Quantity	Units
A	Area	m^2
c	Hydrofoil chord length	m
D	Drag	N
U	Free stream velocity	m/s
ρ	Density	kg/m^3
f	Frequency	Hz
t	Hydrofoil Thickness	Hz
Δu	Velocity deficit	m/s
u	Velocity in x direction	m/s
v	Velocity in y direction	m/s
w	Velocity in z direction	m/s
h	Water tunnel height	m
b	Water tunnel width	m
b_{wake}	Width of wake	m
α	Angle of attack	°
b	Width of water tunnel	m
A_p	Planform area	m^2
L	Lift force	N
D	Drag force	N
p	Pressure	Pa
I	Intensity	−
C	Correlation function	−
μ	Viscosity	kg/(sm)
ξ	Vorticity	1/s
ω	Angular velocity	1/s
ν	Kinematic viscosity	m^2/s
τ_w	Wall shear stress	N/m^2
u_τ	Friction velocity	m/s
f	Relative uncertainty	−

Subscripts

Symbol	Quantity	Expression
max	Maximum	
$norm$	Normalized	

Dimensionless groups

Symbol	Quantity	Expression
Re	Reynolds number	
St	Strouhal number	
C_D	Drag coefficient	
C_L	Lift coefficient	
y^+	Dimensionless distance	

Abbreviations

Symbol	Quantity
PIV	Particle image velocimetry
CFD	Computational fluid dynamics
VG	Vortex generator
LE	Leading edge of hydrofoil
TE	Trailing edge of hydrofoil
CS	Control surface
CV	Control volume
RMS	Root-mean-square
FoV	Field of View
AoA	Angle of Attack
RSS	Root-sum-square

Chapter 1

Introduction

Hydro power is one of the most cost effective and clean energy forms used in the world today. The most commonly used turbine in hydro power plants is the Francis turbine. The longer these turbines can operate the more profitable the power plant becomes. One of the reason for damages in the Francis turbines is the rotor-stator interaction. This is causing an oscillating force on the runner blades due to them passing through the wake of the guide vanes. If the wake of the guide vanes could be manipulated in such a way that the force on the runner blades would decrease this could increase the lifespan of the Francis runner and hence be profitable and good for the environment.
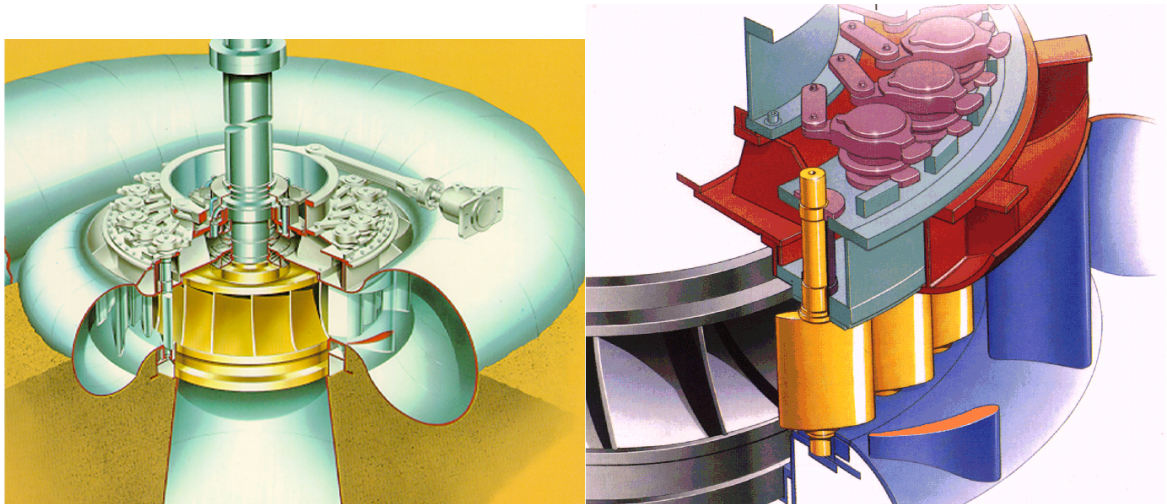
Figure 1.1: Francis turbines. The right figure show the guide vane (yellow) and the runner (gray)

One way of manipulating such flow is by using vortex generators (VGs). The vortex generators can be a physical obstruction mounted on the guide vanes. They are designed in such a way that they are creating a rotational movement in the flow, called vortexes. These vortexes are believed to create mixing between low momentum flow in the wake and high momentum close to the wake and in this way smoothen out the momentum deficit in the wake and in this way reduce the forces on the runner blades.

This work has been motivated by the work of Arnold M. Kuethe and his 1973 patent [9], in which he states that von Kármán vortexes can be suppressed by the formation of stream wise vortexes upstream of the trailing edge. There was given no specific details on the

measurements done. This lead Flow Design Bureau AS (FDB) to do investigations on how vortex generators can be used in flow control.

However, earlier work on wake manipulation is limited. I hope this project can contribute to new insight on how wakes of hydrofoils can be manipulated.

In this project tests are done on a hydrofoil in a water tunnel facility at the University of Minnesota (UMN) in Minneapolis. Particle Image Velocimetry (PIV) are used to investigate how different vortex generators influence the wake of the hydrofoil. A force balance and pressure transducers are used to measure other properties of the water tunnel flow. The results obtained from the experimental work at SAFL are discussed with the help from Computational Fluid Dynamics (CFD) simulation.

For the record, all the measurements and post-processing of the data have been performed by the author.

In Chapter 2 the technical background one need to know to read this thesis is included. In Chapter 3 the experimental work is described proceeded with a presentation and discussion of the results in Chapter 4. The conclusions from this work can be found in Chapter 5 continued by suggestions for further work in Chapter 6.

Chapter 2

Technical Background

In this chapter the theory needed to understand the different aspects of this project is included. As this project is investigating hydrofoil wakes, the technical background will firstly give information about foils and vortex generators. Next, some aspects of wake flow will be described. For an understanding of the forces in our test a section on momentum equation considerations is included. There is also one section with background theory on PIV and CFD, for it to be easier to follow the rest of the report.

2.1 Foil Theory

2.1.1 Hydrofoil with NACA0015 Profile

The hydrofoil that was tested had a NACA0015 profile. The NACA four-digit series is described mathematically, where the first integer describe the maximum value of the mean-chamber line in percent of the chord length c, see Figure 2.1. The second integer describe the distance from the leading edge to the maximum chamber in tenth of the chord length. Foils with zero in the two first integers have equal chambers and are symmetrical. The two last integers describe the maximum thickness t of the foil in percent of the chord length. The thickness distribution is defined as [1, Chapter 6.4]:

$$\pm y = \frac{t}{0.20}(0.29690\sqrt{x} - 0.12600x - 0.35160x^2 - 0.28430x^3 - 0.10150x^4. \tag{2.1}$$
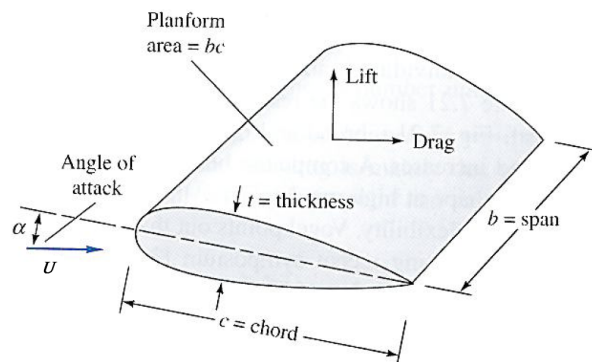
Figure 2.1: Dimensions of a typical lifting vane [18]

The forces working on the hydrofoil when it operates in a flow can be resolved in a drag force D working in the direction of the free-stream flow and a lift force L working perpendicular to the free-stream velocity. These forces are done dimensionless with the definitions [18]:

$$C_D = \frac{D}{\frac{1}{2}\rho U^2 A_p} \tag{2.2}$$

$$C_L = \frac{L}{\frac{1}{2}\rho U^2 A_p} \tag{2.3}$$

where A_p is the planform area of the foil $A_p = bc$.

The angle between the free-stream and the chord line is called the *angle of attack* α, see figure 2.1. In this project the angle of attack have been defines as being negative when the hydrofoil is positioned as in Figure 2.1. The lift and the drag will vary with the angle of attack. The lift coefficient C_L can be predicted from potential and thin airfoil theory [18, chapter 8.7]. For a symmetrical foil this theory give us that:

$$C_L \approx 2\pi\alpha. \tag{2.4}$$

for angles of attack from about $-10°$ to $10°$. The lift coefficients C_L can also be calculated with the foil calculation program XFOIL[1].
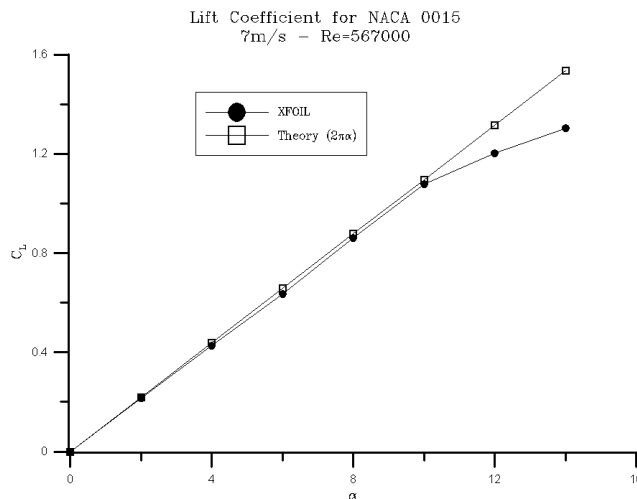
Figure 2.2: Lift coefficient calculated using XFOIL

In Figure 2.2 we can see that expression in Equation 2.4 corresponds well with the calculated C_L for low angles of attack.

The drag coefficient C_D will also increase with angle of attack α. How C_D changes with α can be predicted using XFOIL, as seen in Figure 2.3.

Neither of these predictions take into account the effects caused by the hydrofoil being of finite length, but they will still be a good estimate for the expected lift and drag on our hydrofoil.

---

[1]XFOIL is a free software for the design and analysis of subsonic isolated 2D airfoils. It's available at http://web.mit.edu/drela/Public/web/xfoil/.

Drag Coefficient for NACA 0015
7m/s − Re=567000
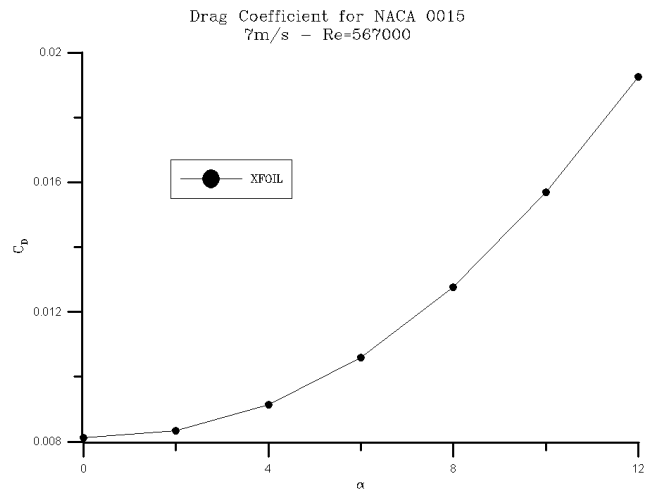
Figure 2.3: Drag coefficient calculated using XFOIL

2.1.2 Vortex Generators

Vortex generators are devices in a flow field that produces rotating movement in the flow. The purpose of the vortex generators in this project has been to mix low momentum flow and high momentum flow in the wake with the goal of smoothing out velocity differences in the wake and the free-stream.

Vortex generators are mostly used in aerospace industry to make the flow over the wings stay attached to the wing for a wider range of velocities and angles of attack, as illustrated in Figure 2.4. Vortex generators will induce drag locally, but can improve the overall performance of the foil in such a way that the total drag will be less than without the vortex generators.
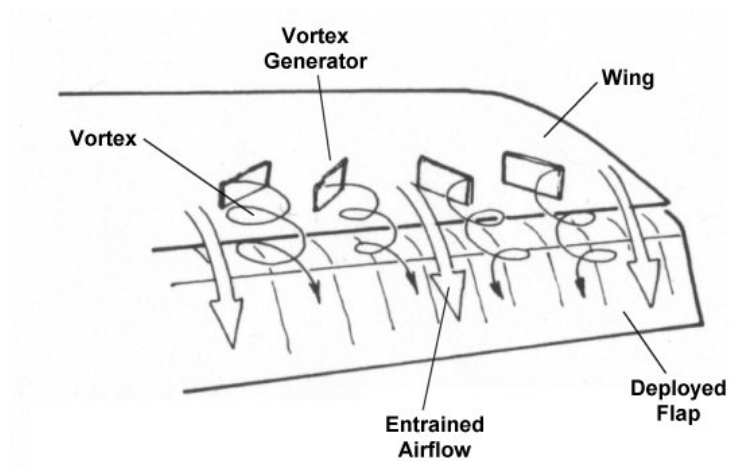
Figure 2.4: The principle of vortex generators [14]

2.2   Wake Flow
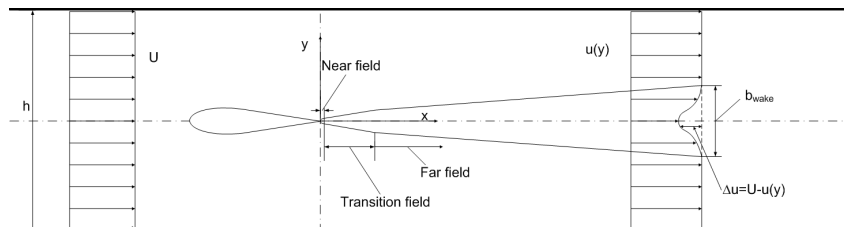
Figure 2.5: Forces on foil and dimensions of wake

Wake flow is the flow downstream of a body that is immersed in a stream. The wake flow can be divided into different zones ([22] and [13]). Close to the body downstream we find the near field, as indicated in Figure 2.5. In the near field the wake flow is very dependent of the shape the body. Further downstream we find the transition field, where most of the momentum transfer between the free-stream and the wake will take place. This changes the form of the wake and evens out pressure gradients. In the far field we find that both the maximum velocity deficit Δu_{max} and the width of the wake b_{wake} will increase regularly with the distance x downstream. By knowing how wake profiles develops, it is easy to compare different wake profiles in the far field as they would look similar when normalized with the maximum velocity deficit and the width of the wake.

In textbooks such as [13] and [19] expressions for how so-called self-similar wake is developing downstream is derived. For the understanding of the appropriate scaling used in this report a summary of this theory is included here.

2.2.1   Development of Turbulent Plane Wakes

The velocity deficit in the wake is denoted $\Delta u = U - u$, see Figure 2.5. The basic assumption is that the velocity profiles far downstream are self-similar, that is:

$$\frac{\Delta u}{\Delta u_{max}} \approx f\left(\frac{y}{b_{wake}}\right) \tag{2.5}$$

where $\Delta u_{max} = f(x)$ and $b_{wake} = b_{wake}(x)$. To arrive at an expression for how the maximum velocity deficit Δu_{max} and the wake width b_{wake} develop downstream the following assumptions must be made:

- velocity defect Δu will be small compared to the free stream velocity U

- there are no pressure gradients other than turbulent pressure fluctuations

- Prandtl's mixing-length assumption for turbulent flow, which makes mixing length proportional to $b_{wake}(x)$

With these assumptions there can only exist a self-similar profile if

$$b_{wake} = const \cdot x^{1/2} \tag{2.6}$$

$$\Delta u_{max} = const \cdot x^{-1/2}. \tag{2.7}$$

It can be shown that this also holds for laminar plain wakes [13] and [19].

2.2.2 Scaling of wake profiles

If we want to compare wake profiles at different distances downstream or wakes from different sized hydrofoils we would have to scale the wake profiles, or else the wake profiles would have different forms at different distances downstream.

When scaling we wanted to make the maximum velocity deficit Δu_{max} and the width of the profile b_{wake} independent of the downstream distance from the foil and also independent of this particular experiment. In this report the same scaling as in [7] will be used:

$$u_{norm} = \frac{U - u}{U} \sqrt{\frac{x}{c}} \tag{2.8}$$

and

$$y_{norm} = \frac{y}{\sqrt{x \cdot c}}, \tag{2.9}$$

where c is the foil's chord length

2.2.3 Approximation of a Wake Profile

When we want to compare different measured wakes it is desirable to have parameters describing the wake. By analyzing measured wake profiles and curve fitting the data to a standard profile this can be done. In the 2003 FDB report [7] the wake profiles have been approximated to follow a standard curve:

$$U_{wake} = a_0 + a_1 e^{-a_2(y_{norm} - a_3)^2}, \tag{2.10}$$

where y_{norm} is defined in Equation 2.9 and the parameters a_0, a_1, a_2 and a_3 can be found by curve fitting the measured profile to the standard curve. This profile will in this project be referd to as the *standard wake profile*. See Figure 2.6 to see how a change in the parameters will change the standard wake profile. This can provide us with comparable parameters for different vortex generator configurations. Note that this wake profile is symmetrical and can not describe unsymmetrical wakes which will be the result when the hydrofoil is at an angle of attack.
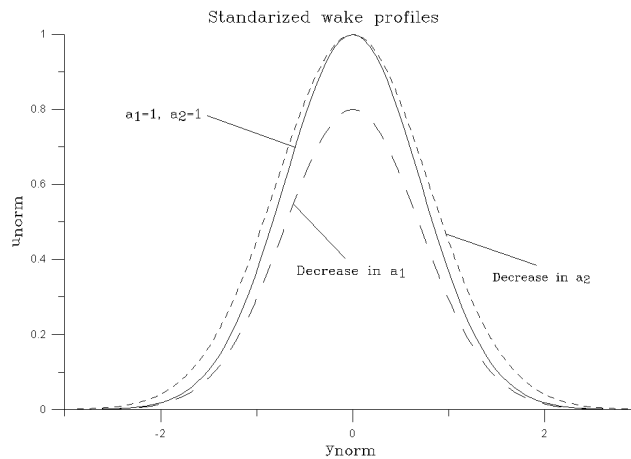
Figure 2.6: The effect a_1 and a_2 have on the standard wake profile

Whether this is a appropriate way of analyzing wake flow has been investigated in this project.

2.3   Momentum Equation

In this section we look into equations describing the forces working on the hydrofoil inside the water tunnel used in the experimental work. We can start off with the stationary impulse version of Reynolds Transport theorem, also called the momentum equation:

$$\sum F_x = \int_{CS} \vec{V} \rho \left(\vec{V} \cdot \vec{n} \right) \, dA$$

We can put up a control volume in the tunnel as shown in figure 2.7.
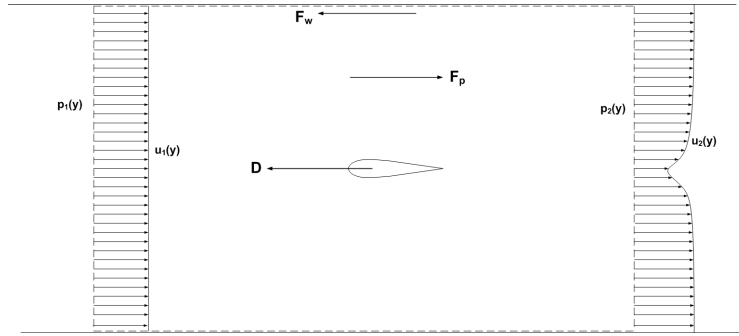
Figure 2.7: Forces involved in the control volume

The forces working on the control volume are the drag force D from the hydrofoil, a pressure force F_p due to the pressure drop over the hydrofoil and a shear force F_w from the walls of the tunnel, as illustrated in Figure 2.7. The cross section of the tunnel shown in Figure 2.7 is more or less equal throughout the width b of the tunnel. With these forces and velocities, the momentum equation becomes:

$$-D + F_p - F_w = -\rho b \int_{-h/2}^{h/2} u_1^2 \, dy + \rho b \int_{-h/2}^{h/2} u_2^2 \, dy \tag{2.11}$$

This is the general momentum equation for our hydrofoil during water tunnel testing. There are many assumptions that can be made regarding the conditions in the water tunnel to simplify the situation. We can assume that the velocity upstream the foil $u_1(y)$ is uniform and equal to the free stream velocity U. This is a reasonable assumption as the average velocity upstream will be very close to the free-stream velocity U, deviating only because the velocity is less very close to the tunnel walls. From this point onwards we will call the velocity downstream u instead of u_2. From the continuity equation we get that $hU = \int_{-h/2}^{h/2} u \, dy$. These assumptions makes it viable to write Equation 2.11 as

$$D = b\rho \int_{-h/2}^{h/2} u \left(U - u \right) \, dy + F_p - F_w \tag{2.12}$$

If this was a free stream the pressure downstream would develop to be equal to that upstream, but as the stream is bound by the tunnel walls we need to take this into account with the pressure force F_p and the shear force F_w. Most textbooks look at the case of free shear flow for which the additional forces F_p and F_w of Equation 2.12 can be disregarded.

2.3.1   Pressure Term of Momentum equation

The pressure force can be found by integrating the pressures upstream and downstream over the cross section of the water tunnel:

$$F_p = b \int_{-h/2}^{h/2} p_1 \, dy - b \int_{-h/2}^{h/2} p_2 \, dy \qquad (2.13)$$

It is, however, difficult to know the variation of the pressure throughout the tunnel. If we are sufficiently far downstream the pressure differences will have evened out and the pressures can be assumed uniform over the cross section of the tunnel. The expression can be further simplified by estimating the pressure difference upstream and downstream with Bernoulli's equation in the "free stream" of the tunnel:

$$F_p = bh \, (p_1 - p_2) = \frac{1}{2} bh U^2 \left[\left(\frac{U_2}{U} \right)^2 - 1 \right] \qquad (2.14)$$

where U_2 is the velocity outside the wake at position 2 downstream the hydrofoil.

The pressure drop in the tunnel is not just due to the hydrofoil. Friction in the water tunnel will also decrease the pressure going downstream. To know how much the pressure drops per length unit in the tunnel, pressure measurements has to be done at different positions going down the tunnel. We do not have such measurements, neither do we know the shear force in the tunnel. Even though it would be interesting to know the size of the drag, it can be just as interesting to know the difference in drag between the different vortex generator configurations.

2.3.2   Impulse Drag

The momentum equation can not be fully resolved by the measurements that were done during the experimental work. Through PIV measurements we could obtain the velocity field in a small part of the tunnel downstream the hydrofoil. We could also measure the velocity upstream. It is desirable to investigate the drag through the information obtained.

This can be done by using a control volume reaching only as high as the cross section of the PIV field of view and letting the control volume boundaries go along stream lines so no water will cross the top and bottom boundary of the control volume. Such a control volume is illustrated in Figure 2.8. The height of the control volume upstream can be calculated through continuity:

$$h_{CV} = \frac{\int_{FoV} u \, dy}{U} \qquad (2.15)$$
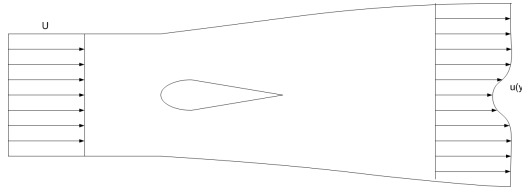
Figure 2.8: Control volume for calculation of impulse induced drag

With such a control volume the velocities across the top and bottom boundaries will be more or less the same, hence the shear force can be ignored in this case. As we do not have any information about the pressure we will consider only the drag and the impulse part of the momentum equation. This gives us the expression

$$D_{imp} = \rho b h_{CV} U^2 - \rho b \int_{PIV} u^2 \, dy = \rho b \int_{PIV} u(U - u) \, dy \qquad (2.16)$$

Even though the true drag D is not known through D_{imp} it can be expected to give us a good indication of the difference in drag from the different tested cases. If an additional drag is caused by a vortex generator, one part of this drag will be found in the impulse term of the momentum equation and another will be found in the pressure term.

By using this expression for the drag we can find the part of the drag coefficient caused by impulse as

$$C_{D,imp} = \frac{D}{\frac{1}{2}\rho U^2 bc} = \frac{2}{U^2 c} \int_{PIV} u(U - u)\,dy \tag{2.17}$$

2.4   Particle Image Velocimetry

The flow visualization technique Particle Image Velocimetry have been used to a large extent
in this project. To understand the experimental work that is done and the discussion of the
results the reader should have some knowledge of PIV. In this chapter technical background
information about PIV is given.

2.4.1   Background

We use flow visualization techniques to get more knowledge about a flow phenomenon. Even
children are experimenting with bark pieces in rivers. In the history of flow visualization
Leonardo da Vinci started out with detailed drawings of structures in flowing water. Later,
in 1904, Ludwig Prandtl started with flow visualization techniques in his own water tunnel.
[11]

Particle Image Velocimetry (PIV) is a flow visualization technique where small particles are
fed into a flow so that photographing of the flow becomes possible. When analyzing the
images of the flow with the particles showing in the photo one can track the particles and
quantify the velocity at different locations.

PIV techniques started in the 80's and evolved with the transition from photo to video
recording techniques. After having recorded the images the calculation of the velocity field
would have to be done manually by tracking the different particles. Later computers have
made it possible to analyze the images and quantifying the velocities automatically, resulting
in a vector fields.
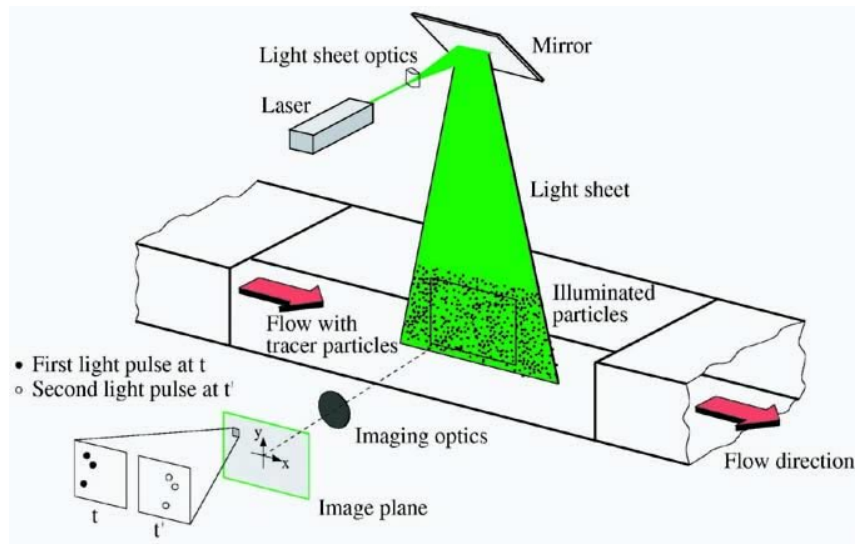
Figure 2.9: Experimental arrangement for particle image velocimetry

2.4.2   PIV Setup

The modern PIV systems consist of a laser and a set of lenses and mirrors producing a
light sheet, see Figure 2.9. A camera will take photographs of the flow and the illuminated
particles. The particles will show up in the image being analyzed using computers. It is
important that the particles added to the flow, called seeding, are small and have a density
close to that of the fluid for the particles to follow the fluid. On the other hand, the particles

have to be large enough to reflect sufficient light to show up in the image. For water liquid experiments a solid seeding material must be used. This can typically be hollow glass spheres or polystyrene, which have a mean diameter of $10 - 100 \, \mu$m.

The photos are taken sequentially with one laser flash for each image, see Figure 2.10. If the time between the flashes is Δt and we can measure that the particles have moved a distance Δs from the images and camera setup, the particle would have had a average velocity in that time of $\bar{u} = \frac{\Delta s}{\Delta t}$.
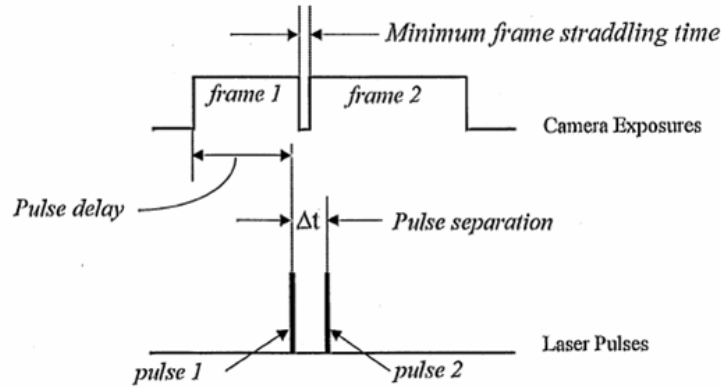
Figure 2.10: The laser pulses and the corresponding image

2.4.3 Image Processing

The process of making vector fields with a computer program is starting by dividing the images into interrogation areas, see figure 2.11. Two interrogation areas from two sequential frames are analyzed using the cross-correlation function. Each image have a intensity field describing the intensity $I(\mathbf{X}, t)$ of the light measured at different position in the interrogation area. The correlation function is described by

$$C(\mathbf{S}) = \int_{spot A, B} I_1(\mathbf{X}, t) I_2(\mathbf{X} + s, t + \Delta t) \, d\mathbf{X}. \tag{2.18}$$

where $\mathbf{S}$ is a two-dimensional displacement vector and 1 denotes the first of two sequentially images, with 2 being the second image. This correlation function can be computed via a two-dimensional Fast Fourier Transform (FFT) of the digitized intensity field:

$$C(\mathbf{S}) = F^{-1} \left\{ F I_1(\mathbf{X}) \cdot F^* I_2(\mathbf{X}) \right\} \tag{2.19}$$

where F denotes a Fourier transform. This analysis results in a cross correlation as shown in Figure 2.11. The cross-correlation peak can be used to find a vector, representing the average flow in that interrogation area. The vectors from each interrogation area can be put together into a vector field.

Several different techniques exists for processing of PIV images, but cross-correlation analysis has appeared far superior, because of better accuracy, noise level and the dynamic range [12].

An important technique when analyzing PIV images is to let the interrogation areas overlap. This can give a higher resolution, i.e. more vectors. It is, however, the size of the interrogation areas that have the greatest impact of the resolution of the velocity field. If the interrogation areas are small there will be less particles in the interrogation areas, which

will increase the error in detecting a valid peak in the cross-correlation [11, Chapter 5.4]. That means, we want the interrogation area to be large enough to avoid cross-correlation errors but small enough to resolve as many of the structures in the flow as possible.

Another important issue when doing PIV recordings is the distance the particles move from one image to another. The uncertainty for the cross-correlation as long as the particles move between 5 to 15 pixels from one image to another [11].

The cross-correlation and the making of the vector field can be programmed on a personal computer, but it is easiest to make the vector fields using commercial PIV software packages, such as DaVis7 by LA Vision or Pivtec.
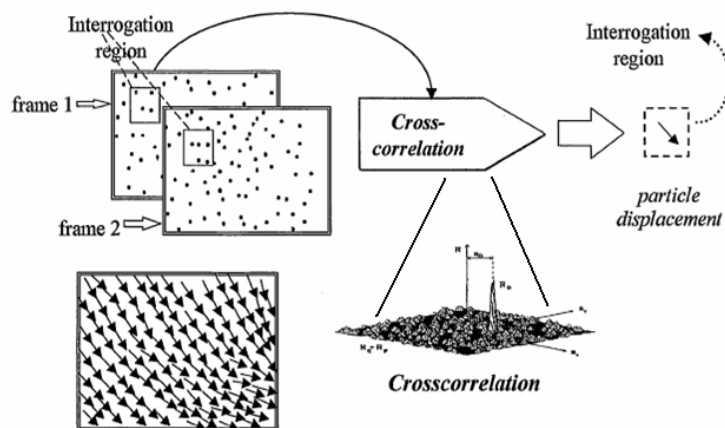
Figure 2.11: The process of image processing

2.4.4   Post-Processing of PIV Data

After the vector field is obtained there has to be done a post-processing of the field, see Figure 2.12. First a validation scheme should be applied to remove outlier vectors and other errors, then a replacement scheme can be applied to fill in missing vectors. Finally the accepted vector field can be further processed to analyze other properties of the flow field.
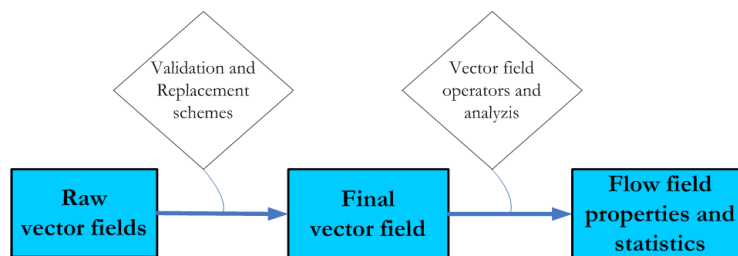
Figure 2.12: The process of vector field processing

Validation and Replacement Schemes

The produced vector fields must be validated using some sort of algorithm. If desired, the missing or removed vectors can be replaced. We can perform the validation and replacement of vectors by visual inspection and calculation, but it is less laborious carried out using a PIV software. Several different algorithms that filters and clean up the obtained vector field exist. One of the simplest removes vectors that are much larger or smaller than it's

neighboring velocity vectors and use interpolation to fill in the missing vectors. In the PIV software there are also filters that can filter out unwanted vectors and use intelligent algorithms to replace them, many described in [10] and [11].

Vector Field Operator Calculation and Analysis   We can use our 2-dimensional vector field to calculate different vector field operators. This can give us additional information about the flow field we are studying. These calculations can be carried out using PIV software, but it may be necessary to make own programs to analyze the data further.

The flow field we are studying will be resolved if the pressure, density and velocity field are known. In that case all terms in the Navier-Stokes equation can be recovered, see equation 2.20

$$\rho \frac{D\vec{U}}{Dt} = -\Delta p + \mu \Delta^2 \vec{U} + \vec{F} \tag{2.20}$$

With our PIV equipment we only measure the velocity field in two dimensions. Even though the flow field can not be fully resolved, the velocity field can be used to find many fluid mechanically relevant quantities.

Turbulent Kinetic Energy   The turbulent kinetic energy give us a quantification of the dynamic part of the velocity field. The velocity can be divided into a stationary and a turbulent part, for the x-direction that would make $u = \bar{u} + u'$. Per unit mass, the turbulent kinetic energy is defined as

$$k = \frac{1}{2} \sqrt{\bar{u'}^2 + \bar{v'}^2 + \bar{w'}^2} \tag{2.21}$$

In our measured vector field we only have information about the velocity in the x and y-direction, hence the last term, w', is ignored when we calculate k. This will introduce an error in the stipulation of the turbulent kinetic energy.

Vorticity and Angular Velocity   One important differential quantity of interest is the vorticity. The vorticity is associated with angular velocity, and is equal to the curl of the vector field:

$$\vec{\xi} = 2\vec{\omega} = curl\vec{U} = \Delta \times \vec{U} = \left(\frac{\partial w}{\partial y} - \frac{\partial v}{\partial z}, \frac{\partial u}{\partial z} - \frac{\partial w}{\partial x}, \frac{\partial v}{\partial x} - \frac{\partial u}{\partial y} \right) = (\omega_x, \omega_y, \omega_z) \tag{2.22}$$

With the components found with PIV we can only find the vorticity in the z direction, ω_z:

$$\omega_z = \frac{\partial v}{\partial x} - \frac{\partial x}{\partial y} \tag{2.23}$$

There are different schemes used to find the vorticity, a good references is [11, chapter 6.4] where other differential quantities are described too.

Divergence and Out-of-Plain Flow   By assuming incompressibility, continuity give us that the divergence of the velocity vector is zero, $\nabla \cdot \vec{U} = 0$, or:

$$\frac{\partial u}{\partial x} + \frac{\partial v}{\partial y} + \frac{\partial w}{\partial z} = 0 \tag{2.24}$$

With our PIV data we know the velocity in the x and y-direction, u and v. Hence we can find the value of $\frac{\partial w}{\partial z}$ as:

$$\frac{\partial w}{\partial z} = -\frac{\partial u}{\partial x} - \frac{\partial v}{\partial y} \tag{2.25}$$

This can be used to detect out-of-plain flow, but it can not be used to recover the out of plain velocity w. This velocity should be retrieved directly through stereo PIV for instance.

Integral Quantities   By integration one can obtain quantities such as circulation, mass flow and stream function, see [11, chapter 6.5].

2.5 Computational Fluid Dynamics

In this project it was carried out a simulation of the hydrofoil in the water tunnel. This section is meant to give sufficient technical background to follow the coming chapters.

2.5.1 Simulation Model and Grid

When simulating the hydrofoil in the tunnel the model should have the same dimensions as the physical system, being big enough to capture the physics we are interested in. One should also make sure that the solution will not be affected by how far the model reaches up and downstream. The model should however, not include too much, as a large model will need more grid cells and hence increase the calculation time.

The grid that we apply to our model have to be sufficiently dense in areas with large gradients e.g. where things change. On the same time the grid can not be too dense as that would make the calculation too heavy and time-consuming. To solve the physics near the walls the grid have to be dense enough close to the walls.

For describing the distance to the wall in a general way it is customary to use the dimensionless distance y^+, defined as:

$$y^+ = \frac{y u_\tau}{\nu} \tag{2.26}$$

where u_τ is the friction velocity at the nearest wall, defined as $u_\tau = \sqrt{\frac{\tau_w}{\rho}}$, ν is the kinematic viscosity and y is the distance to the wall [4].

To resolve the boundary layer completely we need to have at least 10 grid points within the laminar boundary layer with the first one being at $y^+ \leq 5$. Some turbulence models require that there are no grid points inside the laminar boundary layer, and want the grid cells closest to the walls to have a y^+ value larger than 30 but smaller than 300.

The y^+ values of the first grid cells are dependent on the solution, therefore one always have to check the y^+ values of the closest grid points to the walls to validate the grid.

2.5.2 Turbulence Models

We do not have the computing power to calculate each small turbulent eddie, instead we have to use turbulence models describing the statistical nature of the flow phenomenon that we are studying. There are different turbulence models that could be suitable for our simulation. Here are the pros and cons for the different models appropriate for our application ([16] and [4]):

The Realizable $k - \epsilon$ Model

- better than the normal $k - \epsilon$ model for separation, jets and boundary layers.
- will have problems in swirling flows and highly curved boundary layers.

The Reynold Stress Model (RSM)

- very accurate calculation of mean flow properties and all Reynold-stresses for a wide range of flows including wall jets and non-circular duct flow.
- very large computing cost (seven extra partial differential equations) and not as widely validated as the $k - \epsilon$ model.

The Shear-Stress Transport (SST) $k - \omega$ Model

- more accurate and reliable than the standard $k - \omega$ model for a wider range of flows, e.g. adverse pressure gradients and airfoils.

- fail to take account of most subtle interaction between turbulence stresses and mean flow when compared with the RSM

The Spalart-Allmaras model

- shown to give good performance in boundary layers with adverse pressure gradients, which is important for predicting stalled flows. Suitable to airfoil application and is also used in the turbo machinery community.

- is unsuitable for more general internal flows and lacks sensitivity processes in rapidly changing flows.

2.5.3   Main Sources of Error

A CFD simulation can have different error sources. Here are the ones we especially need to look out for:

- Grid: The solution can be dependent of the spacing of the grid element. This can be checked by refining the grid and comparing with the first solution. If the values have not changed significantly, it is likely that the solution is grid-independent. If the solution is changed one can use techniques to estimate what a grid converged solution would be, this could be done by using Richardson extrapolation. When refining the solution one have to make sure that the y_+ values still are within the correct range.

- Physics: We have to be sure that we are modeling the correct physical phenomenon. Questions that needs to be answered are: Is the flow turbulent or laminar? What turbulence model should be used? Is there temperature fluctuations? Is there a second phase and is it significant?

- Discretization of the Partial Differential Equations: The order of solution is that of the first missing term in discretization of the Partial Differential Equations. 1st order can give sufficiently good results in some cases but 2nd order is required for most cases.

- Numerical errors: this can arise from limitations of the software or hardware. If possible to apply double precisions calculation will help

For a guide to verification and validation of CFD simulations see the NASA web page: `http://www.grc.nasa.gov/WWW/wind`

Chapter 3

Experimental

The experimental work that has been done in this project can be divided in the measurements done at the water tunnel facility at SAFL, the post-processing of the measured data at SAFL and the simulation using CFD. The work done in these different parts will be described in the following sections.

3.1 SAFL Measurements

3.1.1 Subjects

We wanted to test how vortex generators influence the wake of a NACA0015 hydrofoil. The hydrofoil was made in brass with tracks made for different vortex generator insets, see Figure 3.1. The tracks for the vortex generator insets are in a distance of $x/c = 0.38$ and $x/c = 0.82$ from the leading edge for respectively the bottom and top surface. The foil was made for the tests series done by Kjeldsen in 2008.

Figure 3.1: The NACA0015 hydrofoil made in brass used in this project

The vortex generator insets are showed in Figure 3.2. They are pointing in an angle of $15°$ to the flow and are $10\,\text{mm}$ long with the pattern repeating each $10\,\text{mm}$. All the vortex generators are $1\,\text{mm}$ high except for one of the V-shaped vortex generators, which is $0.3\,\text{mm}$

Five different hydrofoil setups were tested:

- The Plain NACA0015 hydrofoil, called *plain*

- The hydrofoil with a V shaped $0.3\,\text{mm}$ vortex generator inset in the bottom track, called *VG case 1*

- The hydrofoil with a V shaped $1\,\text{mm}$ vortex generator inset in the bottom track, called *VG case 2*
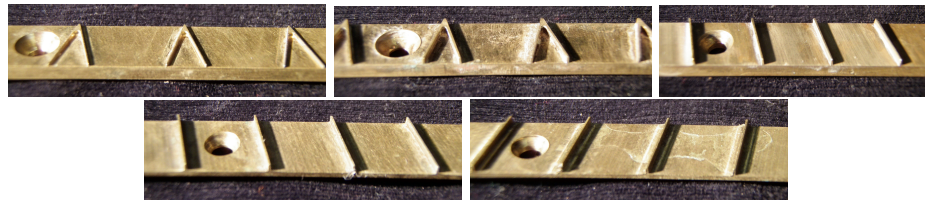
Figure 3.2: The vortex generator insets used in this project. On the top row we have insets for track closest to the leading edge, going from the left we have: V-shaped VG for VG case 1, V-shaped VG for VG case 2 and left pointing VG for the bottom surface for VG case 3 and 4. On the bottom row we have the left and right pointing vortex generator insets for the top surface for VG case 3 and 4

- The hydrofoil with a left pointing 1 mm vortex generator on the bottom surface closest to the leading edge and a left pointing vortex generator on the top surface closest to the trailing edge, called *VG case 3*

- The hydrofoil with a left pointing 1 mm vortex generator on the bottom surface closes to the leading edge and a right pointing vortex generator on the top surface near the trailing edge, called *VG case 4*

Top and bottom surfaces refer to the surface as top and bottom when looking at the hydrofoils shown in Figure 3.1. When saying left and right pointing this refers to the way the vortex generators point upwards, which corresponds to upstream, when looking at the vortex generator insets as in Figure 3.2.

The two last vortex generator have one important difference in design, as case 4 would generate vortexes with the rotational vectors pointing in different directions for the vortexes coming from the top and bottom surface. Whereas case 3 would generate vortexes with rotational vectors pointing downstream for the vortexes created on both surfaces.

All cases was tested at velocities at about 7 m/s and 9 m/s for angles of attack ranging from $-4°$ to $10°$. Positive angles of attack is defined for counter clockwise rotation from alignment with the flow when looking at the hydrofoil as in Figure 3.1.

There was also made one cylinder of 12.7 mm fitting into the water tunnel. This was tested at velocities in steps of 1 m/s from 1 m/s to 6 m/s.

3.1.2 Apparatus

Water Tunnel

The tests was performed at high-speed water tunnel at Saint Anthony Falls Laboratory (SAFL), see Figure 3.3. It was originally built as a free surface test facility but was later modified and is now mostly used for normal water tunnel operation. The pump is controlled by a variable frequency control system installed in March of 2003 together with a 75 hp AC motor [8]. The test section has a length of 1.2 m, a height h of 0.19 m and a width b of 0.19 m. It is possible to observe the hydrofoil in the tunnel from the bottom window and the two side windows. The velocity and the pressure in the tunnel can be regulated independently. The pressure in the tunnel can be adjusted from about 15 kPa to 200 kPa, but low and high pressures result in leakages in the tunnel, making it hard to maintain such pressures stable for a longer time. The measured uniformity of the flow is better than 1 % and the turbulence level is found to be approximately 0.3 % [20].
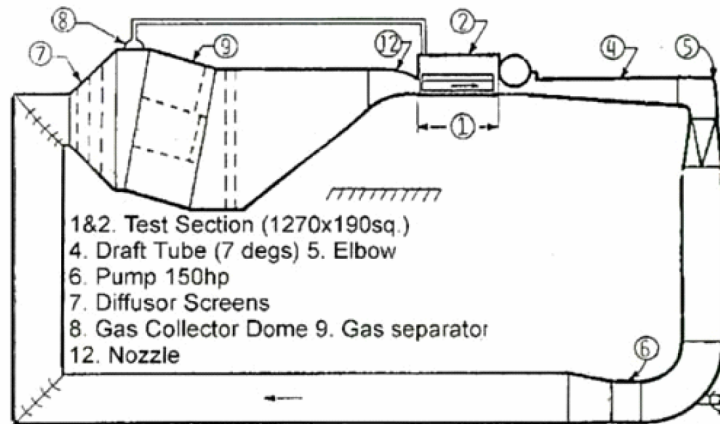
Figure 3.3: The Saint Anthony Falls Laboratory water tunnel

Pressure measurement

During the test there were pressure transducers connected for measuring absolute pressure in the test section and the differential pressure between the settling chamber and the test section. The absolute pressure transducer was of the type Validyne AP10-50 and was connected to the test section 165 mm upstream the center of the hydrofoil.

The differential pressure between the test section and the settling chamber was of the type Validyne DP15-50. It was used to calculate the velocity in the tunnel by using Bernoulli's equation:

$$U = \sqrt{\frac{2(p_1 - p_2)}{\rho}} \tag{3.1}$$

For the test series with the cylinder a Validyne DP15-30 pressure transducer was connected to a tap 330 mm downstream the center of the cylinder. This measured differential pressure between the upstream and downstream tap.

Force balance

The force balance that was used was made during Kopriva's [8] master thesis in 2006. The force balance got a spider connection and a momentum arm for taking away any unwanted moments on the load cells, see Figure 3.4. The lift measurement is done by the load cell getting load transferred through the spider near the mounting plate, while the the drag measurement is done by the load cell getting load transferred through the lift load cell connected to a slider, separating the lift and drag measurement. As the drag is small compared to the lift this will not affect the lift measurement noticeable. The lift was measured with an Omega LC501-200 load cell and the drag was measured with an Omega LCDA-100 load cell. The accuracy of the force balance for lift and drag was reported by Kopriva [8] to be 3 % and 2.7 %, respectively, based on full-scale measurements of 900 N lift and 100 N drag.

PIV Equipment

The PIV equipment that was used was composed of a Nd:YAG laser (Neodymium: Yttrium Aluminum Garnet), Photonics DM30-527. This laser can deliver pulses with energy content
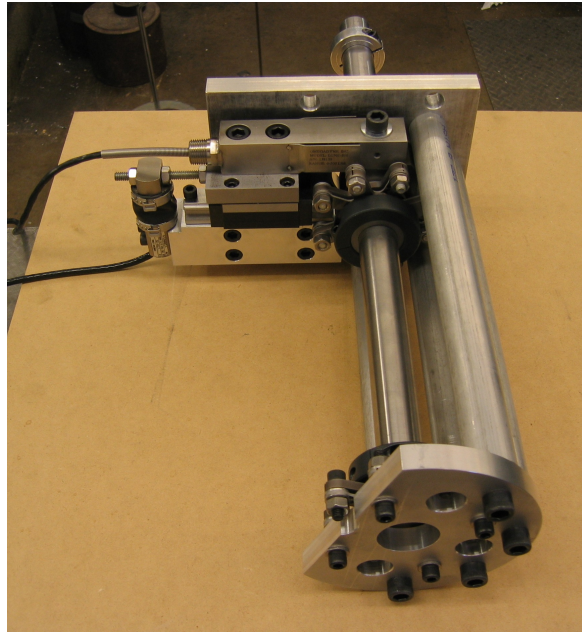
Figure 3.4: The force balance used at the SAFL water tunnel

of $10 - 400\,\mathrm{mJ/pulse}$. The seeding used was hollow glass beads. For taking the photos a high speed camera of the type Fastcam APX-RS was used. This can take images at a frequency up to $10000\,\mathrm{Hz}$. When taking images at $10000\,\mathrm{Hz}$ the resolution of the image could be up to 512 by 512 pixels. If taking images at lower frequencies we can use higher resolution. The lens that was used for the high speed camera was a $105\,\mathrm{mm}$ Nikon lens.
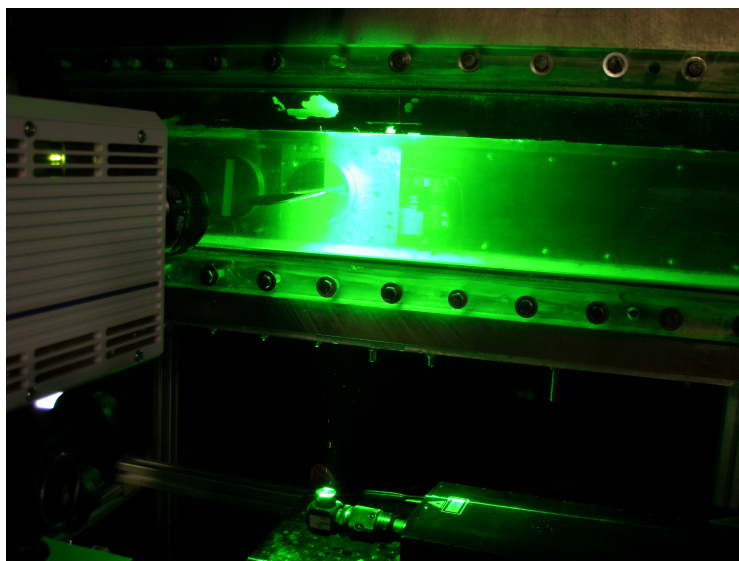
Figure 3.5: Setup of PIV equipment at the SAFL water tunnel

Data Acquisition Hardware

The pressure and force measurements were done with a PC with a standard data acquisition program made in LabView where one could adjust the frequency and number of samples of the recording. All the PIV recordings were done with another PC with the DaVis7 software installed.

3.1.3 Procedure

Calibration and Preparation

Before starting the PIV recording the system had to be calibrated. This was done by placing a calibration plate, Figure 3.6, with a grid of points in a known distance inside the test section just downstream the hydrofoil in the plane of the laser. After filling the tank with water to get the same refraction as under test conditions, it was taken a picture with the system, making sure that the trailing edge of the hydrofoil showed up in the photo. The image was analyzed with the DaVis7 software to get the length scales right.
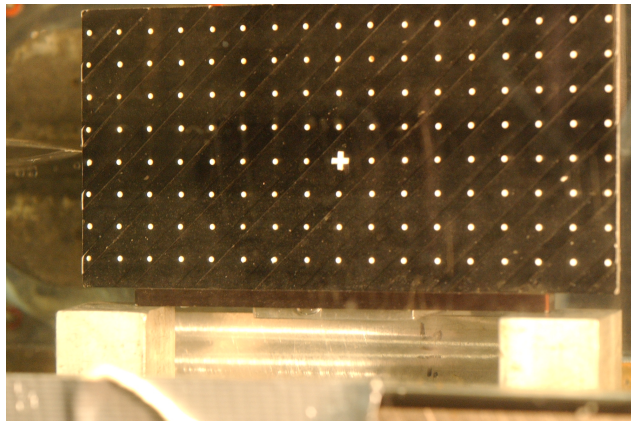
Figure 3.6: The PIV calibration plate

In the coordinate system that was chosen to use for the PIV measurements, origo was defined to be at the end of the trailing edge of the hydrofoil at an angle of attack of 0°, as in Figure 2.5. After having calibrated the PIV equipment the derived coordinate system had to be translated to coincide with our defined origo. This was also done with DaVis7 by pointing out where the end of the trailing edge was in the calibration picture, which included the hydrofoil at an angle of attack of 0°.

To post-process the PIV images it was important that the particles did not move too far from one image to another. For the hydrofoil recordings there were taken 1000 images at 10000 Hz with a resolution of 512x512 pixels. This made the particles move between 8-12 pixels from image to image. The field of view corresponded to an area of about 50x50 mm just downstream the trailing edge. The laser plane was selected so it would fall exactly in between the V shaped vortex generators. For the left pointing vortex generators the laser plane would cross the physical vortex generator, see Figure 3.7

The pressure transducers were calibrated using mercury manometers, according to standard procedures at SAFL. As the atmospheric pressure changed from day to day, the calibration curve for the absolute pressure had to be adjusted according to the atmospheric pressure of that specific day.

The load cells was calibrated using known forces. As the lift was calibrated using known

Figure 3.7: The laser plane and the NACA0015 hydrofoil

weights, we had to assume that an equal upward force would give an equal absolute voltage. The drag load cell was calibrated using a fish scale, increasing the tension and reading the fish scale measured force. The errors due to the calibration are negligible compared to the offset errors that was observed during tests.

Performing the Tests

Before running tests it was made sure that both velocity and pressure oscillations in the tunnel had dampened out. The measurement of the pressures and forces were done at 1000 Hz, and taking the average of 1000 samples. The recordings had to be started manually on the two computers. For this reason the PIV images and the other measurements can have been taken with a time difference of maximum 10 seconds.

For high velocities and high angles of attack cavitation occurred on the hydrofoil because of the low pressure on the suction side of the hydrofoil. As cavitation would disturb the wake flow in study, it was decided to increased the absolute pressure in the tunnel until cavitation disappeared.

Originally it was planned to run tests at angles of attack of $12°$ too, but the lift force working on the hydrofoil was so large that the rod transferring the force got physically stopped by the mounting plate. For this reason the lift measurement would have been wrong for such a high angles of attack. Finally, it was decided to only run testes up to $10°$.

The PIV camera and the laser was inside a curtain to avoid light from the lab to disturb the recording and to protect our eyes from the laser. When changing angles of attack on the hydrofoil it was a chance of touching the curtain and by that disturbing the camera, making it move just a little bit. This would cause the coordinate system to be somewhat displaced. Even though the correctness of the coordinate system was checked regularly it is not sure that the camera have been in the same position during all tests. By studying the PIV images and comparing the location of the trailing edge to origo we find that the coordinate system have had an offset of as much as 2 mm in the y-direction, and as much as 1 mm in the x-direction. However, the coordinate system can not have moved during the recording time so the calculated velocities have not been affected by this. The origin of the coordinate system can, have small errors from test to test.

The cylinder cases had pressure and force measurement recorded continuously for 40000 samples at 10000 Hz for capturing the dynamics of the system. The PIV recording was done

with different frequencies making the particles move about 8-10 pixels from image to image for the different cases.

3.1.4 Experimental Design and Analysis

Design of vortex generators

In aerospace industry vortex generators have mainly been used to control boundary layer separation. To make the drag induced by the vortex generators as small as possible it has been customary to use a vortex generator height in order of the boundary layer thickness.

When the first set of tests using vortex generators for mixing of the wake was done at SAFL in 2003 by FDB, the vortex generators was designed so that the vortex generator height should exceed that of the boundary layer thickness in order to achieve an effect on the wake [7]. Vortex generators of two different heights were designed, 1 mm and 0.3 mm, to see the effect this would have on the wake. It was chosen to make the new vortex generators the same heights so that tests from 2003 could be compared with the new test series.

To have base case to compare the vortex generator with, it was decided to test a plain NACA0015 hydrofoil, this was done by using smooth insets.

To run tests at the cylinder was motivated by the need to have a base case for shedding frequency investigation. As the expected frequency for the cylinder is roughly known.

After the test for the hydrofoil had been carried out, it was observed that the drag measurement had poor accuracy. When it was decided to run a test series with the cylinder it was believed that the drag could be calculated using the pressure difference from upstream and downstream the cylinder together with PIV measurements. This proved later to be less accurate than expected.

Thus it was decided to measure the differential pressure between upstream and downstream the cylinder. This would both give us the pressure drop and the pressure oscillations (another way of finding the shedding frequency).

The processing and analysis of the PIV measurements will be described in the following

3.2 Vector Field Calculation and PIV Post-Processing

3.2.1 Subjects

The vector field calculation is done on the recorded PIV images as seen in Figure 3.8. Further on the vector fields are post-processed. This processing can be performed at any time after the PIV recordings are done, and is a separate process from the the PIV measurement itself, even though it can be done using the same software.
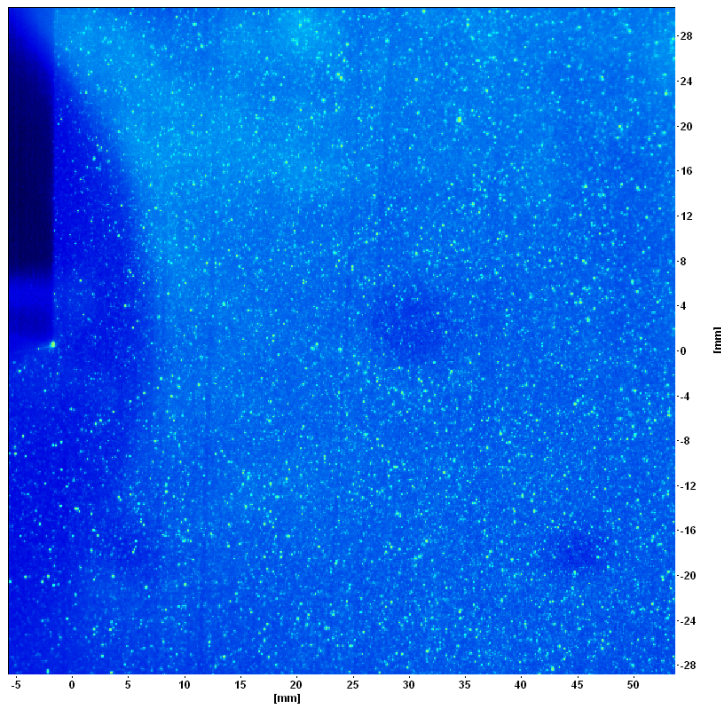
Figure 3.8: PIV image

3.2.2 Procedure

The PIV software, DaVis7 by LAVision, was used to calculate the vector fields, do the validation and replacement on the vector field, to filter further and generate other interesting properties. After this, own Matlab programs was made for doing more customized studies on the wakes. The procedure can be divided into processing done with DaVis7 and processing done with Matlab.

Processing Done with DaVis7

In DaVis7 there are many different types of post-processing that can be made. After having tried many different analysis schemes on the PIV images a description of the most appropriate combination have been made. This post-processing include the following steps:

- Extracting a rectangle of the PIV image for vector field calculation (see Figure 3.9 top left)

- Calculation of vector fields with a validation and replacement algorithm (see Figure 3.9 top right)

- Smoothening the vector field with an non-linear filter (see Figure 3.9 bottom left)

- Calculating the vorticity strength (see Figure 3.9 bottom right)

- Calculating the average velocity field

These schemes are standard algorithms in DaVis7 but the parameters have to be selected correctly for each individual image series. Especially for the vector field generation one have to take into account aspects described in Section 2.4. The procedure used for each step is described under.

Extracting a Rectangle   The extraction of the rectangle was done for two reasons. First of all, the vector field would be disturbed if the laser shadow from the hydrofoil showed up in the PIV image. The second reason is that calculating the vector field for the whole image takes a long time when it is done on 1000 images, about 1 hour. To reduce the time needed for the vector calculation we extract only the area of interest, the wake downstream the foil.

Vector Field Calculation   The parameters and algorithms sat for the vector field calculation is extremely important for obtaining any result of value. It was chosen to use cross-correlation between each sequential image.

For processing the vector fields DaVis7 first analyze a large interrogation area, e.g. 64x64 pixels, to get an idea of the velocity field in question. When analyzing the large interrogation area an overlap of 50 % was used between the interrogation areas to get higher resolution. The large interrogation area ensured accurate peak detection in the cross-correlation The produced vector field is used for knowing more or less where the particles are moving, this improves the cross-correlation on smaller interrogation areas, e.g 12x12.

The size of the smallest interrogation area was for most processing sat to be 6x6 pixels. If the vector field appeared chaotic in time a larger interrogation area had to be used.

The validation scheme that was used remove vectors with difference to the average of the neighboring vectors larger than 3 times the RMS[1] of the neighboring vectors. The replacement scheme fill up empty spaces in the vector field by interpolation.

Smoothening With Non-Linear Filter   This filter helps to replace spurious vectors from the vector field by calculating a predicted value for each vector taking into account gradients of second order [10].

Vorticity Strength   DaVis7 has a function that calculate the vorticity strength. The vorticity strength is used instead of vorticity as it showed to give better visualization. The visualization of vortexes is very sensitive to the selection of interrogation area. Whether the interrogation area should be small or large depends on the size of the vortexes involved in the velocity field. If the interrogation area is too small, vortexes inside the main vortex structure will show up and the general appearance of the vorticity field will be very unstable. Moreover, if a too large interrogation area is used the vortexes that show up will be incorrect. Once a suitable interrogation area is found one has the possibility of using a smoothening algorithm that makes the visualization of the vorticity better. Setting the smoothing parameter to 0.5 was found to make the best visualization.

Average Vector Field   This is done by DaVis7 to get the average of a whole test series. It is easier to calculate the average field in DaVis7 than programming such a program yourself in Matlab or LabView.

---

[1]RMS refers to the root-mean-square operation [17]
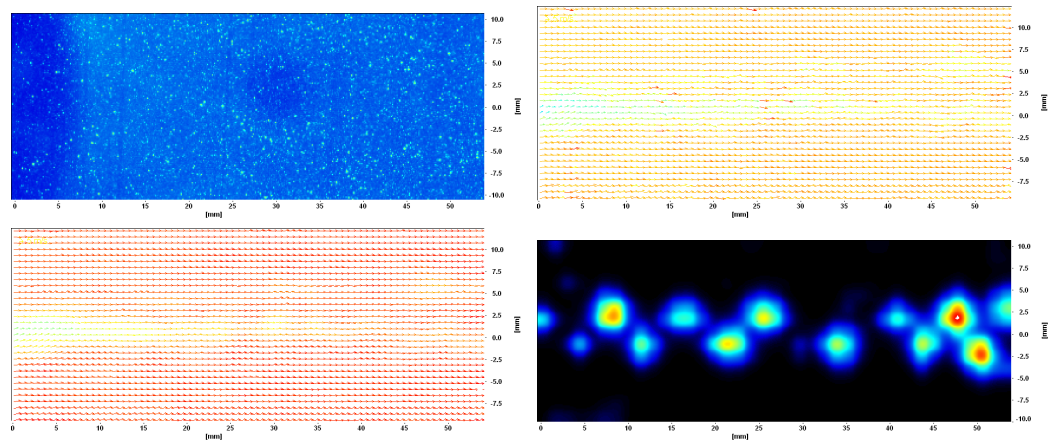
Figure 3.9: PIV post-processing steps

Processing Done with Matlab

Many weeks of programing were carried out prior to the test period at SAFL. Programs where made in Matlab so that the results could be analyzed fast and tests could be redone if necessary.

Before the many possibilities in DaVis7 had been explored some more weeks of programming were laid down to make average vector fields and analysis schemes for vorticity which already existed in DaVis7. It turned out to be easier to do as much processing in DaVis7 as possible and then export the wanted result to *.dat* files and finally reading the files into Matlab.

Early on, a program was made for curve fitted the measured wake profiles to the standard wake profile, Equation 2.10, described with the parameters a_1 and a_2. The curve fitting was done by using a Matlab function that was using a least-square method. Some of the early programs was developed using measurement data from 2003 of a plain hydrofoil.

Many different programs were made, some just for getting the same scale on the different results produced in DaVis7 and others to calculate drag properties or calculate the out-of-plane movement. Some approaches worked well others did not, on the way many new ideas for how to best analyze the data was developed.

3.3 CFD

CFD was used in this project to examine some of the physical effects observed during the tests. Because there was no pressure measurement done downstream the hydrofoil it would be interesting to find qualitative how the pressure distribution would be in the tunnel. Another aspect of interest was how the velocity was outside the field of view for the PIV.

3.3.1 Choosing Turbulence Model

When choosing turbulence model for the simulation the different models in Section 2.5 was looked into. As computing time was an important issue together with the wish to use a widely validated model for foil calculations the Spalart-Allmaras model was chosen, see Section 2.5.2.

3.3.2 CFD Model and Grid

The water tunnel tests was simulated with a 2D CFD model. This assumes that effects like wall friction at the side walls and tip losses can be ignored, which is not totally correct but can give a good description of what is going on in the water tunnel. The height of the tunnel was set to be 190 mm and the length of the hydrofoil was set to be 81 mm, as in the physical model. The length of the CFD model was sat to be about 5 times the chord length upstream and 15 times the chord length downstream, see figure 3.10. After getting a solution this was tried increased to see if that would change the solution, which it did not do notably.
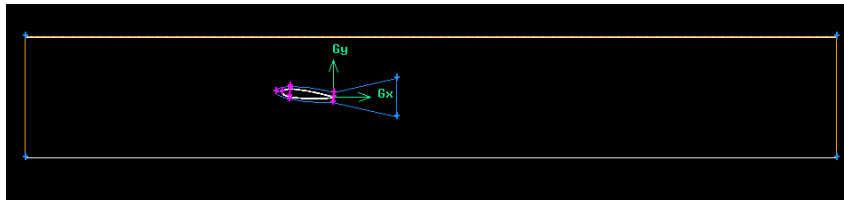

Figure 3.10: The CFD model used for the hydrofoil at 6°

The NACA0015 profile was obtained by first calculating the different coordinate points with a Matlab script using the definition in [1], see Section 2.1.1. These points were then written to a *.dat* file and then read into Gambit 2.4.6. Using these points a 2D models of the hydrofoil in the tunnel could be made at 6° and 0°. The models were drawn and meshed using Gambit 2.4.6.

When using the Spalart-Allmaras model one have to choose whether to resolve the boundary layer or not. To resolve the boundary layer it is suggested that the grid cells closest to the walls have a y^+ value in the order of 1 and at least less than 5.

It was decided to resolve the boundary layer, hence the actual proximity of the first grid cell to the wall had to be calculated. This can be estimated by using the definition of y^+ in Equation 2.26 and $u_\tau = \sqrt{\frac{\tau_w}{\rho}}$ [13, Chapter 17.1]. The calculated drag coefficient from XFOIL gives a drag of about 3 N for $u = 7$ m/s and 0° which give a shear stress, the shear force per unit area, of about 100 N/m². To have the first grid point at an y^+ value in the order of 1 the grid point should be about 0.003 mm from the wall. This was obtained in Gambit by using the boundary layer function for the hydrofoil and the tunnel walls.

The area around the hydrofoil was divided into separate regions, see Figure 3.11. This was done to make it easier to mesh the area with a denser and structured grid close to the
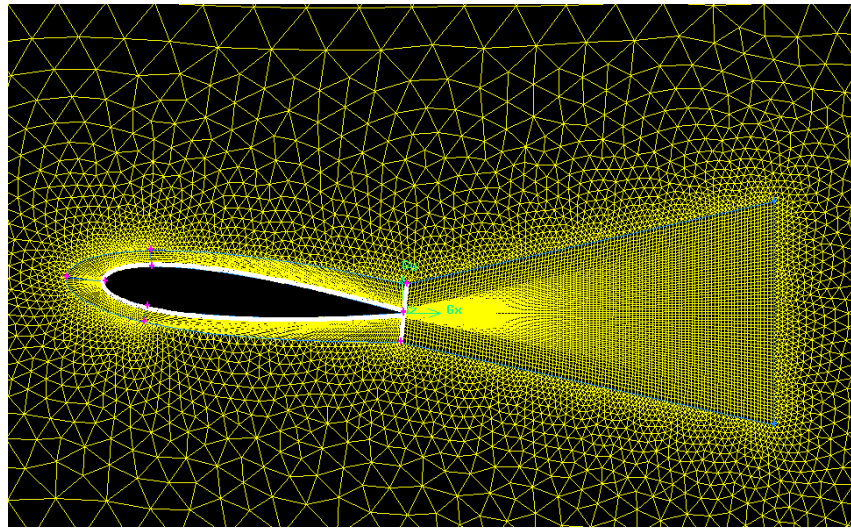
Figure 3.11: The grid used for the hydrofoil at 6°

hydrofoil. We need to have a dense grid in areas with gradients, which is expected to be around the hydrofoil and in the wake. This is easy to control with a structured mesh, which was used in the regions of interest.

3.3.3   Solving the model

The grid was imported to the commercial CFD software Fluent, where the model was solved.

The gradient option was switched to Green-Gauss Node Based, as suggested in The Fluent Help Pages [4]. This is for better numerics, in particular for unstructured meshes, it is also supposed to predict drag more accurately. Strain/Vorticity Based Production was selected as suggested in the Fluent Help Pages [4] when using the Spalart-Allmaras model.

The inlet was sat to velocity inlet with a uniform speed of $7\,\mathrm{m/s}$ and the outlet was sat to be outflow. I sat the fluid to be water, which can be assumed incompressible as velocities are much less than the speed of sound in water. As we first of all is interested in average properties of the flow, a stationary CFD simulation was done. Making the residuals get to less than 10^{-4}. After the solution had converged to a stationary state, including the forces on the hydrofoil, the grid was adapted according to the y^+ values. In this way the grid was refined in wall areas with y^+ values higher than 4. This was done until all y^+ values were within the accepted range.

To check that the grid was dense enough, a doubling of the grid was done in Fluent. However, the properties of interest did not change much with the refined grid. Hence no further refinement of the grid was performed. The convergence and the y^+ values for the final simulation at 0° can be seen in Figure 3.12.
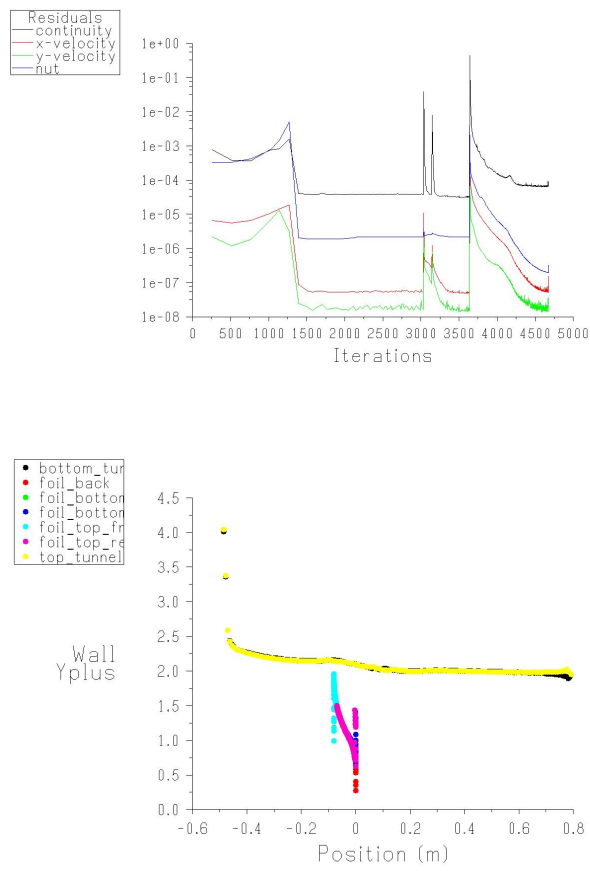
Figure 3.12: Residuals and y^+ values for CFD simulation of the hydrofoil at 0°

Chapter 4

Results and Discussion

In this chapter the results from the experimental work is presented with a discussion of the results.

In the first section the flow field of the water tunnel is explored, mostly through the use of CFD. Next the drag measurements are presented with a discussion of the results. To investigate the drag further, the use of $C_{D,imp}$ is discussed. After this section the lift measurement is looked into, followed by a discussion on the use of the standard wake profile.

One large section is devoted the different findings in the wake properties of the different vortex generator cases. After this the energy conservation in the wake is looked into. This chapter will end with a discussion of the uncertainties involved in the work presented.

4.1 Investigation of the Water Tunnel Flow Field

4.1.1 Velocity Distribution

To gain more insight into what is happening inside the water tunnel, a CFD analysis of the plain hydrofoil test of $7\,\mathrm{m/s}$ was carried out. In this simulation the velocity field was calculated, shown in Figure 4.1.
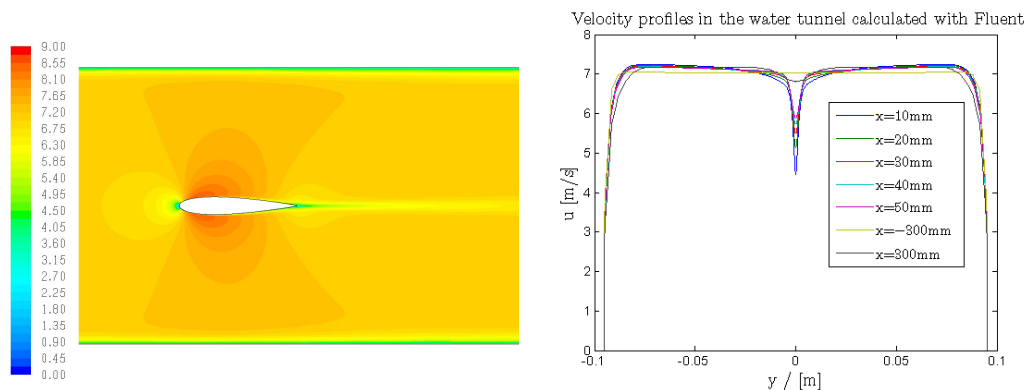

Figure 4.1: Velocity field calculated with CFD

On the top in this figure we get an idea of the velocity field in the tunnel. The velocities seams to be fairly constant outside the wake and close to the hydrofoil. In the lower figure information have been extracted from different lines going through the tunnel at different

x-positions, $10\,\mathrm{mm}$, $20\,\mathrm{mm}$, $30\,\mathrm{mm}$, $40\,\mathrm{mm}$, $50\,\mathrm{mm}$, $-300\mathrm{mm}$ and $300\mathrm{mm}$. We can see that the velocity in the "free-stream" downstream the hydrofoil is not constant but is changing with y-position.

4.1.2   Pressure Distribution

One of the assumptions for the self-similar wake found in Section 2.2 is that there is no pressure gradients in the wake. Through the CFD simulation I could investigate this assumption. The result is shown in Figure 4.2. It is easy to see that there are pressure gradients in the field of view of the PIV measurement. This will cause the wake to develop differently than described in Section 2.2.
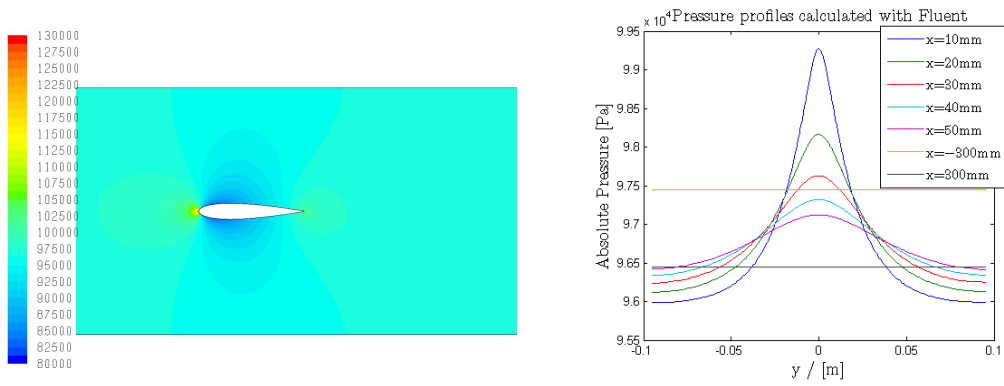

Figure 4.2: Pressure field calculated with CFD

Another aspect with the pressure distribution in the water tunnel is the pressure drop in the x-direction, as described in Section 2.3.1. It is expected to be both a pressure drop due to the hydrofoil, but also a pressure drop throughout the water tunnel due to friction at the tunnel walls.

The pressure drop over the hydrofoil can be visualized by plotting the absolute pressure at a line going from upstream the hydrofoil to downstream the hydrofoil. In Figure 4.3 the absolute pressure along a line at a x position of $80\,\mathrm{mm}$ is plotted. It is noteworthy that the pressure drop has not stabilized before we get about $200\,\mathrm{mm}$ downstream the hydrofoil. This indicates that the far field is further downstream than the field of view of the PIV measurement.

From the CFD analysis the pressure drop in the water tunnel is found to be $1140\,\mathrm{Pa/m}$. As illustrated in Figure 4.3 the pressure drop from 0.3m to $-0.3\,\mathrm{m}$ is $1000\,\mathrm{Pa}$. The pressure drop due to tunnel friction is $780\,\mathrm{Pa}$ leaving $320\mathrm{Pa}$ to be due to pressure drop over the hydrofoil, seen as the gap in Figure 4.3

During the tests, it was believed that by inserting a pressure transducer that could measuring the pressure drop from upstream to downstream the hydrofoil the pressure term of the drag could be found. With such a measurement we would get the pressure drop resulting from both pressure drop over the hydrofoil in addition to the pressure drop in the tunnel.
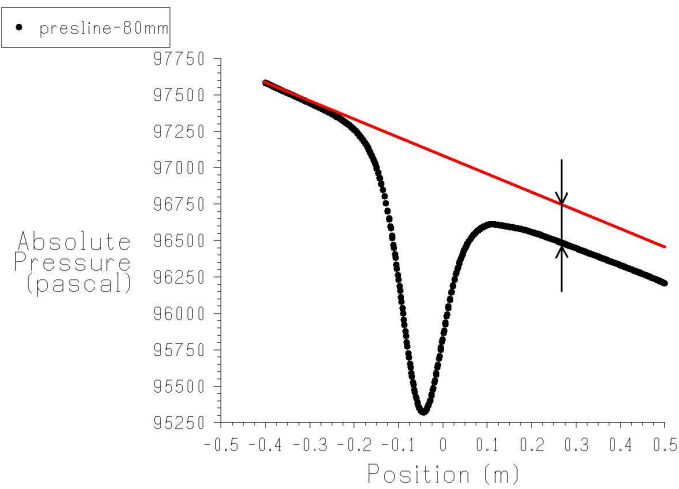
Figure 4.3: Velocity field calculated with CFD

4.2 Drag Investigation

4.2.1 Measured Drag

The drag was measured with the force balance. It was desirable to investigate the quality of the measurement. This was initially done by comparing the the measured drag to data calculated by XFOIL for the plain hydrofoil, see Figure 4.4. There is a dip in the drag for angles of attack from 2° to 6°. The drag measured at $u = 7\,\mathrm{m/s}$ has got the same shape, indicating that the dip is not due to measurement uncertainty. The reason for this behavior is not known, but it is believed to be related to how flow conditions at the tip of the hydrofoil are changing with angles of attack.

Figure 4.4: Measured drag coefficients for plain NACA0015 hydrofoil compared with XFOIL calculation

The drag was measured for all angles of attack and all test cases, with the result shown in Figure 4.5. As illustrated in the figure, some of the data points seem to be invalid.

As the drag coefficient for the plain hydrofoil change similarly with α for the two velocities.

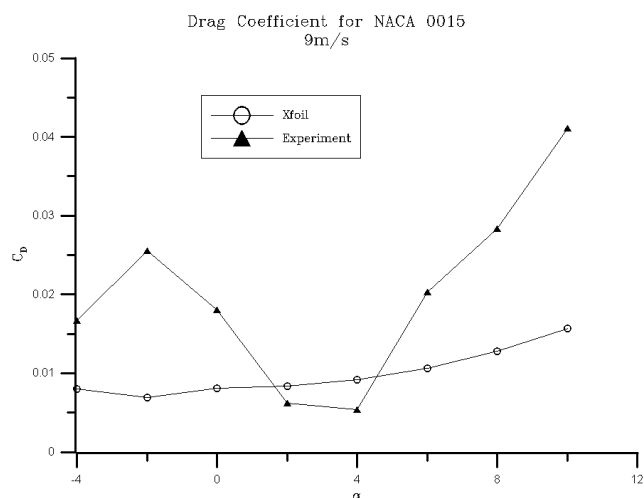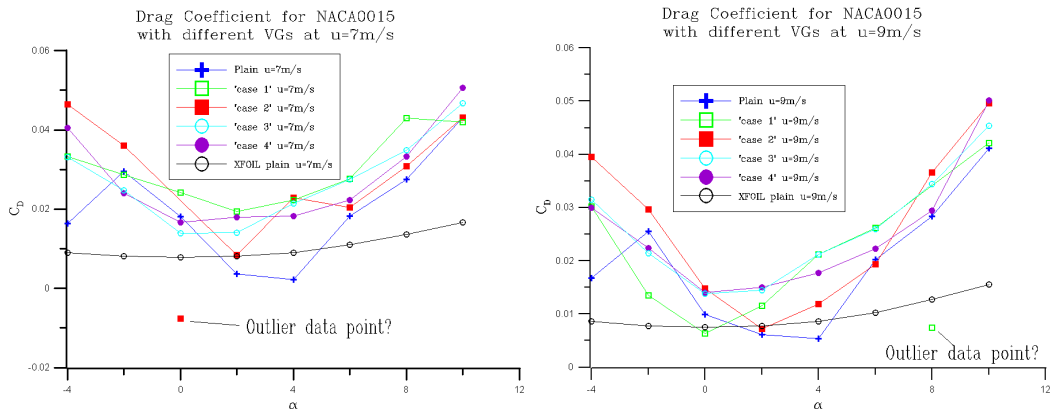Figure 4.5: Measured drag coefficients at different angles compared with XFOIL calculation, for 7 m/s and 9 m/s

This measurement is unlikely to have outlier data points. By knowing this, one way to compare the operation of the different vortex generators would be to subtract the drag coefficient of the plain hydrofoil from the drag coefficient of the other cases. This would give us a relative drag coefficient. To make trends easier to detect the outlier data point shown in Figure 4.5 was removed. The result can be seen in Figure 4.6.
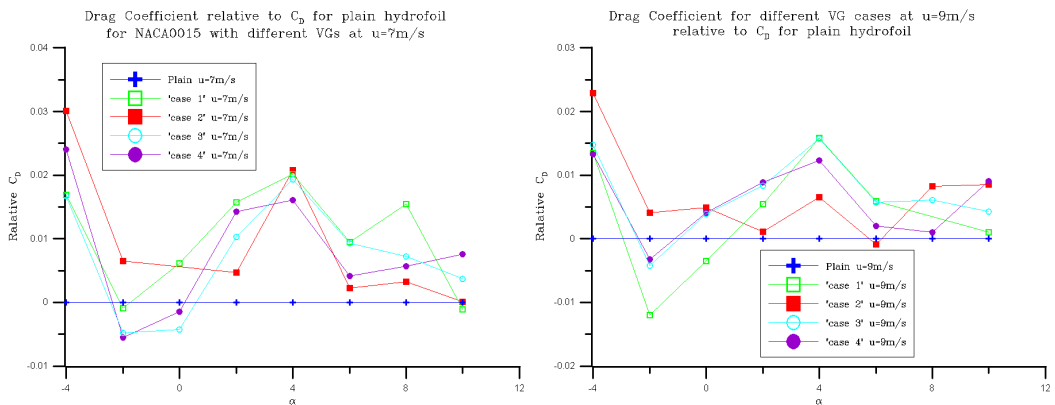
Figure 4.6: Drag coefficients relative to the plain hydrofoil as a function of angle of attack, for 7 m/s and 9 m/s

All the vortex generators will introduce some increased drag locally, but vortex generators can keep the flow attached and in this way reduce the total drag. The need to keep the flow attached is expected only for higher angles of attack and hence the use of vortex generators should in general increase the drag, which also is seen for most tests.

For negative angles of attack the VG's being closest to the leading edge will be on the pressure side of the hydrofoil. For small angles of attack the flow will stay attached and hence the vortex generators on this side can be expected to increase the total drag. VG case 1 has the larges area seen from upstream and can be expected to cause the largest drag. This is also seen in Figure 4.6. Other than this, it is hard to make any general conclusions on how the vortex generators will affect the drag from the force balance measurement.

4.2.2   Drag investigation with CFD

As the difference in drag between the different vortex generator cases could not be determined, it was necessary to investigate other means of comparing drag. This was hoped to be possible by looking at the velocity deficit in the wake and calculating the impulse part of the drag, $C_{D,imp}$.

The CFD analysis is not sure to report the correct drag on the hydrofoil, but it is likely to report correctly whether a in angle of attack reduce or increase drag. This could be used to check how the impulse part of the drag was related to the actual drag, see Section 2.3.

This was done by comparing the drag reported reported by Fluent with the impulse part of the drag calculated from wake profiles. In this way $C_{D,imp}$ would be calculated as for the PIV measurement, and it could be seen how a change in C_D could expect to change $C_{D,imp}$. In the PIV wake the $C_{D,imp}$ can be evaluated with control volumes having the downstream boundary at different x-positions. The same can be done for the wake from the CFD simulation.

In Figure 4.7 C_D and $C_{D,imp}$ are compared for the CFD simulations of the hydrofoil at an angle of attack of $0°$ and $6°$ at $7\,\mathrm{m/s}$. In the figure the corresponding calculation resulting from PIV measurement is included. The reference C_D is in this case based on the drag measured by the force balance. The $C_{D,imp}$ is changing with x-direction as it is calculated with control volumes reaching downstream to different x-positions.

It is interesting to see that $C_{D,imp}$ becomes negative as the control volume is extended downstream, this means that the missing part of the drag, the pressure term, will make up for the apparently changing drag.
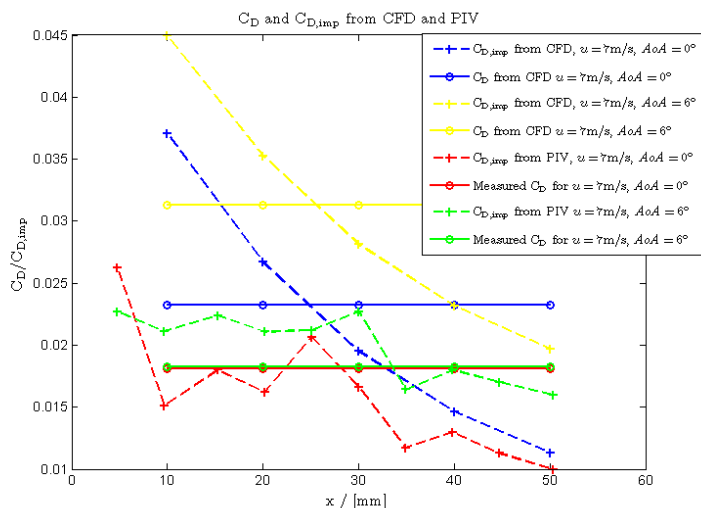
Figure 4.7: Drag coefficients and impulse part of drag coefficients from CFD and PIV

From the CFD analysis it is found a higher drag coefficient than what was found in the water tunnel. This can be due to the use of a too high wall roughness in the CFD simulation. The CFD simulation is reporting a higher drag coefficient for higher angles of attack, which also was reported in the XFOIL analysis shown in Figure 2.3. The drag measured with the force balance does not show the same correlation. In general the force balance have had very bad repeatability, which very well can be due to hysteresis. On the other hand the calculated $C_{D,imp}$ show good agreement with the expected increased drag for higher angles of attack. I hence argue that the use of $C_{D,imp}$ is more appropriate to evaluate the change in drag between the different cases tested than the force balance.

4.2.3 Calculated drag from PIV data

Seeing that $C_{D,imp}$ can be a viable measure of differences in drag, $C_{D,imp}$ was calculated for the different vortex generator configurations. In Figure 4.8 this is calculated for the different cases at an angle of attack of 0° and $U =$ m/s.
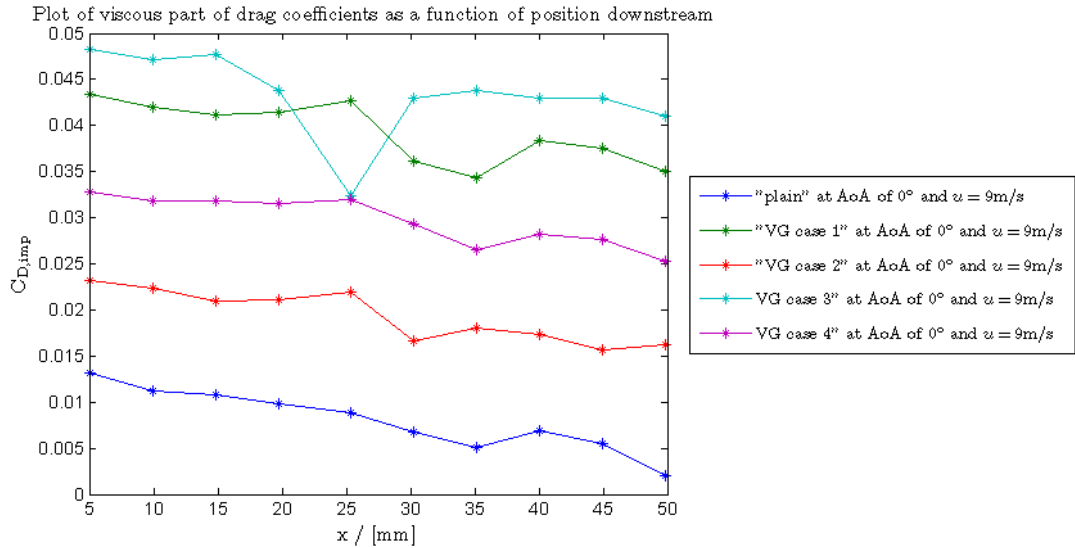
Figure 4.8: Part of Drag coefficient caused by velocity change

The plain hydrofoil shows to causing less drag than the hydrofoil with vortex generators. This is expected as the vortex generator will be an additional obstruction in the flow at an angle of attack of 0°.

The same calculation was done for for the test cases at 6° and $U = 9\,\text{m/s}$. The result is shown if Figure 4.9.
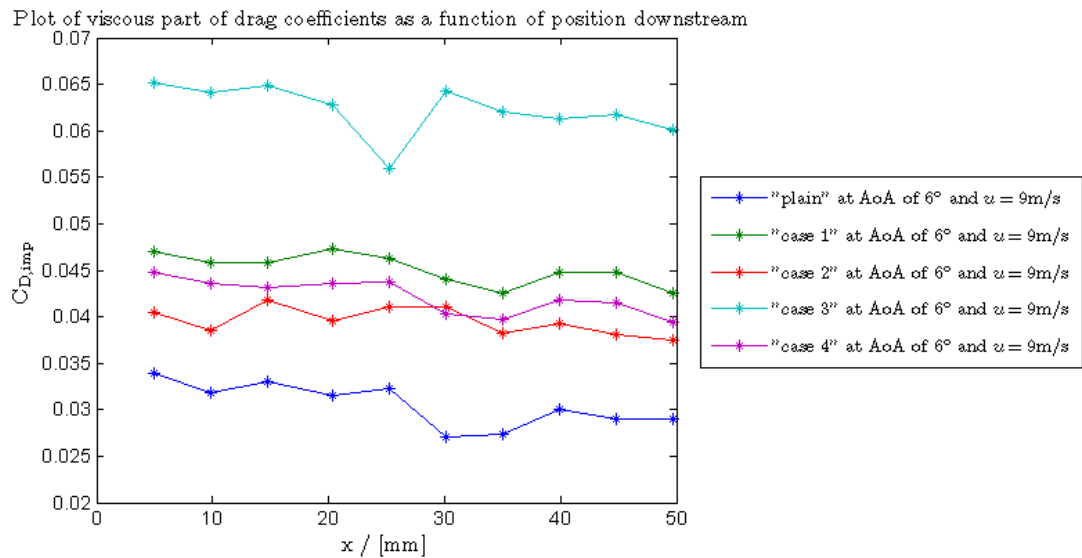
Figure 4.9: Part of Drag coefficient caused by velocity change

The calculation of $C_{D,imp}$ indicates that the drag is largest for the vortex generator case 3

followed by case 1 and 4. It vortex generator case 2 have less drag than any of the other vortex generators cases tested.

Because the post-processing of the the PIV data is very time consuming I had no time to investigate how the vortex generators performed at other angles of attack. For this reason it is not known whether the drag properties is a general effect or just valid for these analyzed cases.

4.3   Lift Investigation

The lift was measured with the use of the force balance. The lift force is many orders larger than the drag force, hence there is less uncertainty in the lift measurement than the drag measurement. How the measured lift coefficient changes as a function of angle of attack can be be seen in Figure 4.10. In this figure the lift coefficient for the NACA0015 profile calculated with XFOIL is included. For the test of the VG case 1 at $u = 9\,\mathrm{m/s}$ there seems to be an outlier data point at $8°$, as for the drag measurement.
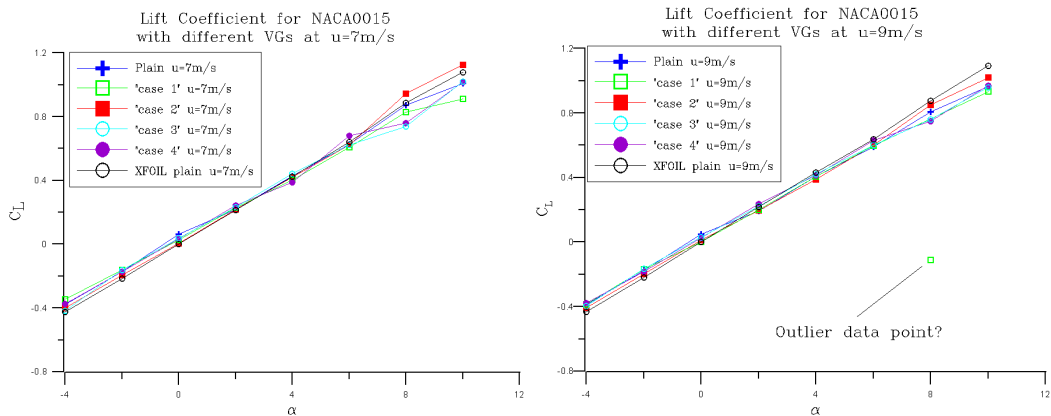
Figure 4.10: Measured lift coefficients for plain NACA0015 hydrofoil compared with XFOIL calculation

To compare the different VG cases the lift coefficient measured for the plain hydrofoil was subtracted from the drag coefficients for the VG cases. This result can be seen in Figure 4.11, where the outlier data point shown in Figure 4.10 is removed.
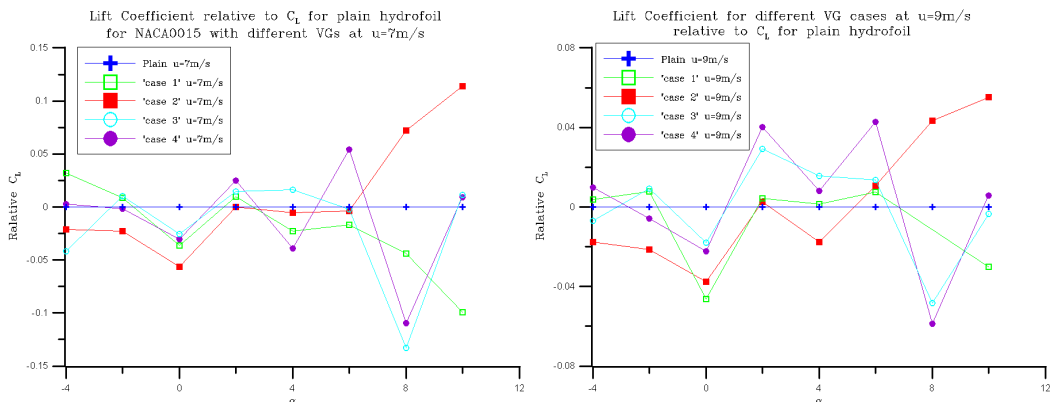
Figure 4.11: Measured lift coefficients for plain NACA0015 hydrofoil compared with XFOIL calculation

The relation between the different VG cases seems to be similar for both velocities. In general the lift coefficients of the VG cases behaves similar to that of the plain hydrofoil. But at higher angles of attack the operation changes. VG case 1 seems to have a lower lift coefficient than the plain hydrofoil. VG case 2, which is similar to VG case 1 only being higher, gives higher lift at higher angles of attack than the plain hydrofoil. The reason for this difference in operation is not known.

The VG cases 3 and 4 are giving lower lift than the plain hydrofoil for an angle of attack of $8°$ but gives about the same lift as the plain hydrofoil at $10°$. The reason for this is not

known.

The lift can also be found by calculating the circulation around the hydrofoil. However, there is not sufficient information from the PIV analysis to perform such an analysis.

In conclusion the VGs will affect the operation of the hydrofoil some in terms of lift.

4.4 Investigation of the Standard Wakes Profile

The idea of normalizing the wakes and fitting them to a standard wake profile, Equation 2.10, was meant to make it possible to compare many different cases with a common standard and easily comparable parameters. Before we could start using this scheme to compare tests it had to be investigated how well the standard wake profile could describe the measured wake profiles.

This was investigated by plotting normalized velocities from different cross sections of the wake downstream. It turned out that the velocity profiles did not lay exactly on top of each other as expected, but had an offset in velocity and in y-position, see Figure 4.12. The offset in y-position can be both be due to the coordinate system having an offset, as commented in Section 3.1.3, and the hydrofoil having an angle of attack causing the wake to translate in y-position downstream. The offset in velocity, seen in Figure 4.12, is caused by the wake being inside a water tunnel and not in a unbounded free shear flow. The velocity outside the wake downstream will have to be higher than the velocity upstream because of the velocity deficit in the wake. This will cause the normalized velocity to be negative outside the wake. Apparently, the difference between the "free-stream" velocity upstream and downstream is changing with x-position.
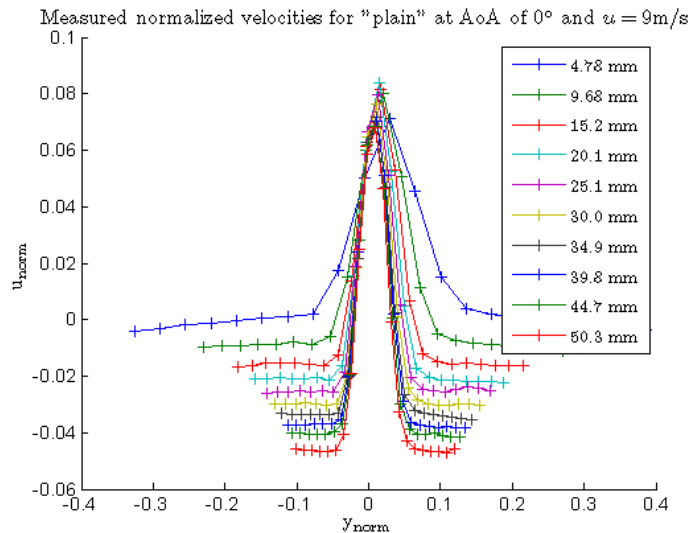

Figure 4.12: Normalized wakes without adjusting for velocity or y-position offset

Before a curve fit could be applied on the wake profiles the offsets had to be removed. To remove the offset in y-position the position of the lowest velocity in the wake was found and subtracted from the original position. The velocity offset was taken care of by calculating the mean velocity of the flow outside the wake for each position downstream and using this velocity instead of the free stream velocity upstream the hydrofoil.

After closer thought, it would have been a better idea to use the velocity outside the wake for calculating the normalized wake profiles. This would have been a better representation of a wake in an unbounded flow. Instead it was decided to remove the offset.

After removing the offsets one could start curve fitting the standard wake profile to the normalized measured profiles. For the plain hydrofoil and VG case 1 the measured wakes could be described very well with the standard wake profile, see Figure 4.13. The standard wake profile is symmetrical, hence it can only describe wakes for no or very low angles of attack this close to the trailing edge.

On the other hand the standard wake profile showed to describe the wakes of the hydrofoil
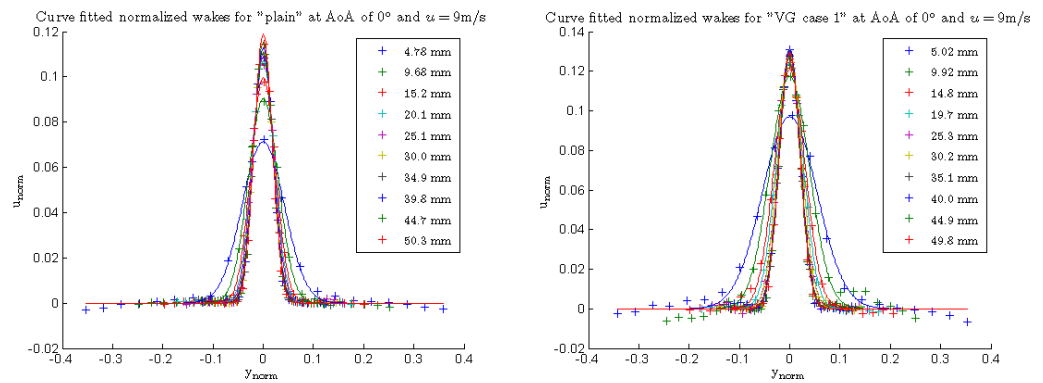
Figure 4.13: Measured PIV data in good agreement with standard wake profiles

with other vortex generators quite bad, see Figure 4.14. We see that using vortex generators is causing the wake to be unsymmetrical. As it is believed that the wake will eventually develop into a self similar shape, it is apparent that the field of view for the PIV measurement was not in the far field of the wake fore these vortex generators.
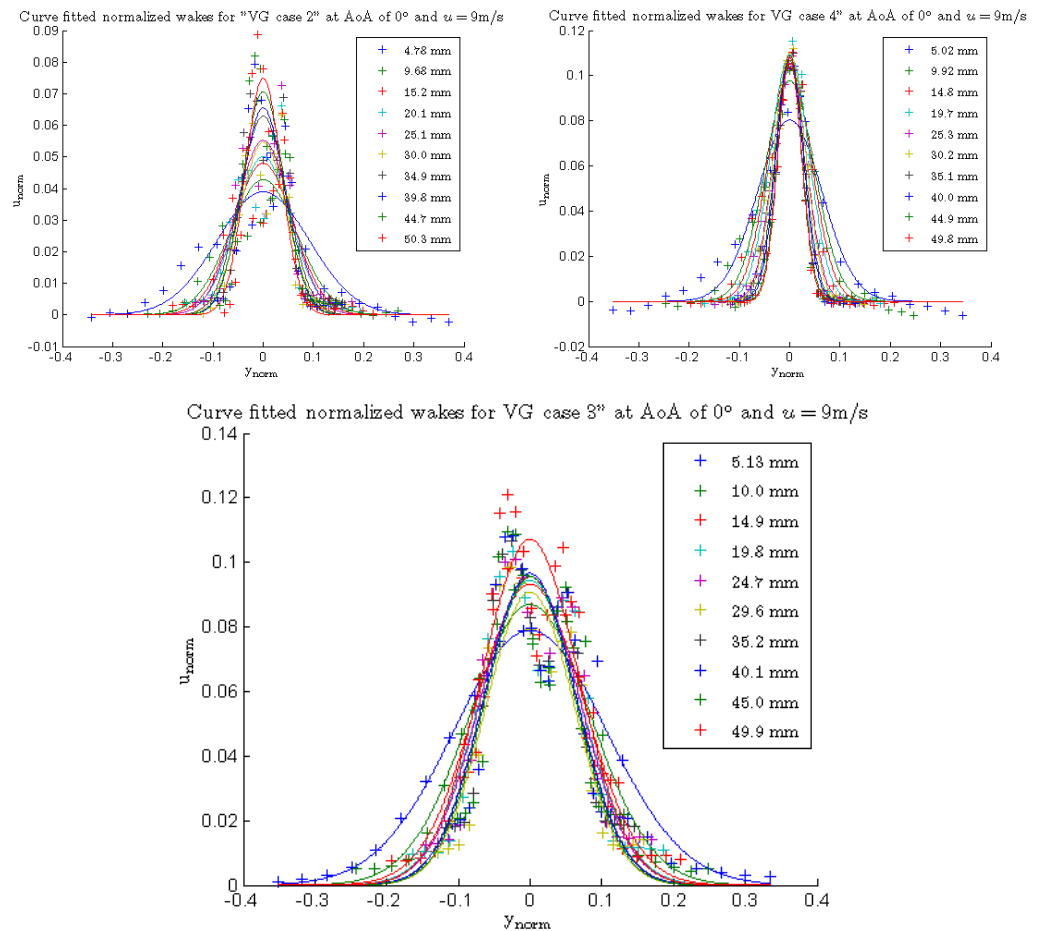
Figure 4.14: Measured PIV data in poor agreement with standard wake profiles

I also investigated whether the wakes really had developed into the self-similar shape in our

field of view for the two cases that could be well described by the standard wake profile. If the wakes were self-similar the coefficients in the standard wake profile should be a constant independent of the position downstream where the wake was evaluated. The result is shown in Figure 4.15. Here we can see that the coefficients a_1 and a_2 are changing with the position downstream, which indicates that the wake is in the transition field and is still not in the far field.
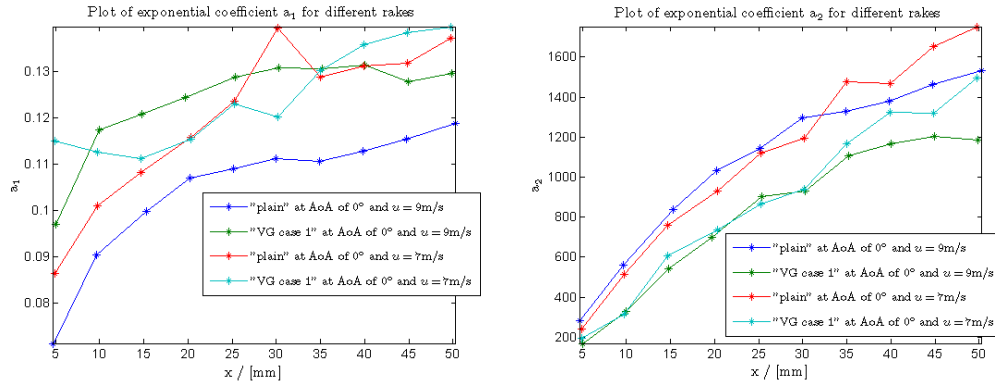
Figure 4.15: Coefficients of the standard wake profile curve fitted to measurements

In conclusion we can say that the standard wake profile is not appropriate to use for comparing the different vortex generator cases tested in this project. However, the use of the standard wake profile should not be disregarded, as it is believed that the wakes will eventually develop into a form similar to the standard wake profile.

4.5 Wake Manipulation

When investigating the operation of the different vortex cases post-processing techniques described in Section 3.2 have been used.

4.5.1 Investigation of Wake Velocities

When starting to compare the different vortex generator configurations normalized velocities was investigated. For the calculation of the normalized velocity (Equation 2.8) the measured free stream velocity upstream was used. This velocity was found through the differential pressure transducer, using Bernoulli's equation.

In this investigation of the normalized velocities the offset of velocity and position has not been removed as discussed in Section 2.2.3. This was for better visualization of the blockage effects caused by the tunnel. For the plain hydrofoil and the vortex generator case 1, see Figure 4.16, we see that the velocity deficit is kept more or less constant downstream. Note that the same scale is used on all the plots of normalized velocity for easier visual comparison. The maximum normalized velocity $u_{norm,max}$ is higher for case 1 on the same time the wake is wider, this indicates that the there is an increased drag caused by the vortex generator.

From Figure 4.16 we also see that the velocity outside the wake just downstream the hydrofoil is about the same as the velocity upstream U, $u_{norm} = 0$, but when moving further downstream it becomes larger than U, causing the normalized velocity to become negative.
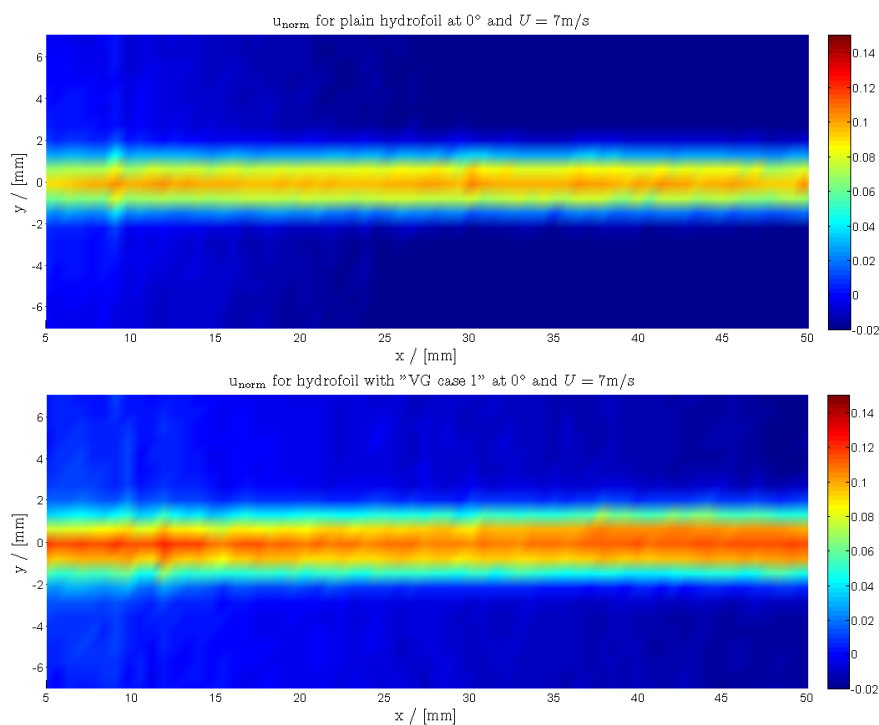
Figure 4.16: Normalized velocity in the wake of the plain hydrofoil and VG case 1

This normalized velocity was evaluated in the same manner for the CFD simulation for the $0°$ angle of attack at $7\,\mathrm{m/s}$, as seen in Figure 4.17. The lines in the figure represent the field of view of the PIV measurement, with 10mm distance between the lines.

As the normalized velocity will be complex for negative x-values I had to define u_{norm} with the absolute value of x in Fluent, hence the field is only valid downstream the trailing edge.

We see that the normalized wake profiles are similar for the CFD simulation and the PIV measurement, Figure 4.16. However, the wake velocity calculated by CFD seems to be somewhat less than the measured velocity. This indicates that the roughness constant was too high in the CFD simulation causing the calculated drag to be higher than the measured drag, which also was seen from the drag investigation.

Figure 4.17: Normalized velocity field calculated with CFD

When looking at the normalized velocities for the vortex generator case 2, Figure 4.18, we see that the wake is much more smoothed out and the maximum velocity deficit is much less than for the plain foil. For both vortex generator cases 1 and 2 the VG is placed on the bottom side of the hydrofoil, 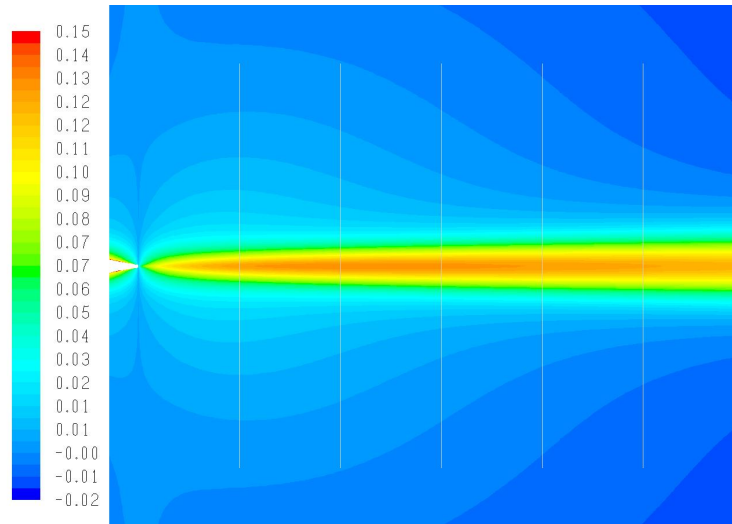at negative y. As there is an uncertainty in the y-position of the field of view, as described in Section 3.1.3, it can not be known for sure whether the reason for the wake being at a high y-position is due to the vortex generator or the displacement of the coordinate system.
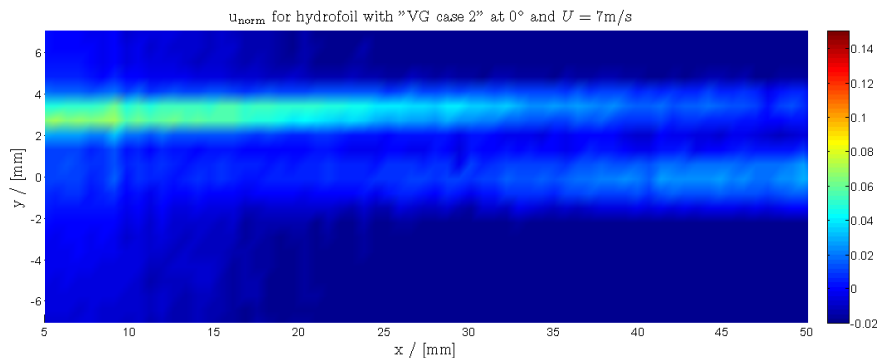
Figure 4.18: Normalized velocity in the wake of the hydrofoil with VG case 2

Figure 4.19 show the wakes from vortex generator case 3 and 4. This figure show that there is a huge difference from having vortex generators making vortexes that go in the same or opposite directions. VG case 3, which makes the vortexes rotate in the same direction, appear to make the flow from the top and the bottom of the hydrofoil repel each other. On the other hand VG case 4, which makes the vortexes rotate in opposite directions, appear to make the flow from the top and the bottom of the hydrofoil to merge. This is making the wake almost as thin as for the plain hydrofoil. This merging also seems to make the velocity

deficit larger than for the plain hydrofoil, but this could also be caused by increased drag by the vortex generators.

Figure 4.19: Normalized velocity in the wake of the hydrofoil with VG case 3 and 4

4.5.2   Out of Plain Flow

The out-of-plane flow can be investigated through Equation 2.25. When looking for out-of-plane flow we have to think carefully about how the vortex generators are working. A left pointing VG on the top surface will induce a swirl going clockwise when looking in the x-direction. A left pointing vortex generator on the bottom surface of the hydrofoil will induce a swirl going in the same direction. Such a combination correspond to VG case 3.

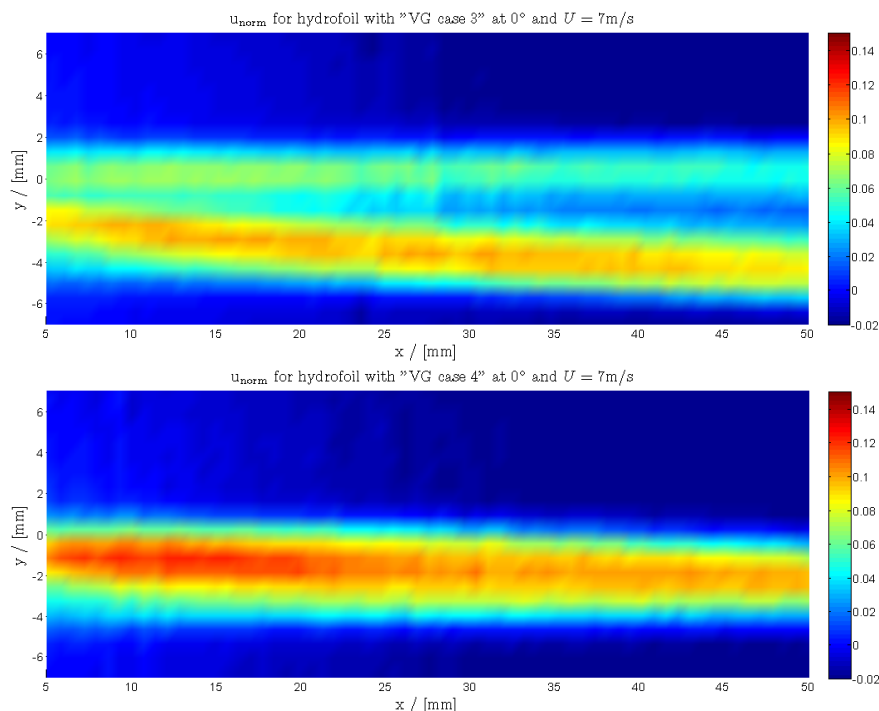When looking at the hydrofoil as in Figure 2.5 and defining positive z-direction towards the reader a swirl going in positive z-direction will experience an acceleration working against it's movement and hence loose velocity in z direction, said in another way $\frac{\partial w}{\partial z} < 0$.

This is seen when looking at the plot of $\frac{\partial w}{\partial z}$ for the hydrofoil with VG case 3 at an angle of attack of 0° and $U = 9$m/s in Figure 4.20.

For this vortex configuration the VG at the top surface is left pointing and hence is producing a clockwise vortex when looking in the x-direction. The upper part of this vortex is moving out of the PIV plane in positive z-direction. This part of the vortex will will have negative $\frac{\partial w}{\partial z}$, and can be seen as the blue part in the figure. The part of the vortex going in negative z-direction have a positive $\frac{\partial w}{\partial z}$ and is seen as red in the figure. Because we have left pointing vortex generators on the bottom surface for this VG case, there is another vortex moving clockwise a bit lower. Hence we see two swirls systems working in the figure.

This analysis can give us much information on how the generated vortexes are interacting downstream. For case 3 the vortexes seem to be transforming into a larger vortex going in the same direction as the two original swirls.

When looking at the plain hydrofoil in Figure 4.21 we can see that there is less out-of-
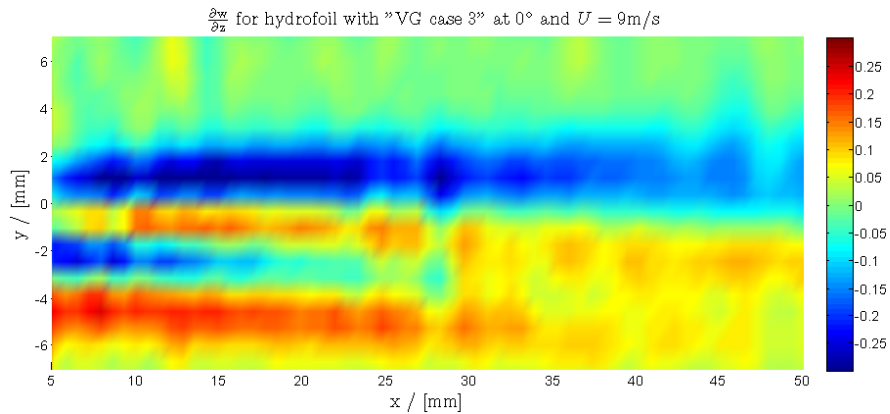
Figure 4.20: Out of plane flow visualized with $\frac{\partial w}{\partial z}$ for "Case 3" at an angle of attack of 0°
and $U = 9$m/s

plane flow, which is expected as the flow should be more or less two-dimensional over this
hydrofoil.

Figure 4.21: Out of plane flow visualized with $\frac{\partial w}{\partial z}$ for "Case 3" at an angle of attack of 0°
and $U = 9$m/s

Case 2 had V-shaped vortex generators on the bottom surface of the hydrofoil. The plain
of view was placed just in between two V-shaped VG's. It is hard to know how the two
vortexes will interact as they go downstream, but in the field of view of the PIV there seems
to be one large vortex going counterclockwise when looking in the x-direction, figure 4.22.

This is, however, not seen for VG case 1, shown if Figure 4.23, which seem to have little out
of plane flow. These vortex generators are also V-shaped but are shorter than for VG case
2. We could expect less out-of-plane flow, which is seen, but I can not explain what seems
to be a weak vortex structure going in the opposite direction from that seen for VG case 2.

For VG case 4 there are right pointing vortex generators on the top surface of the hy-
drofoil generating vortexes going in a counter clockwise direction when looking in the the
x-direction. On the bottom surface there are left pointing vortex generators inducing vor-
texes in clockwise direction when looking in x-direction. Figure 4.24 show that this VG case
also have a out-of-plane flow pattern, but I have yet to propose an explanation for this.

Figure 4.22: Out of plane flow visualized with $\frac{\partial w}{\partial z}$ for "Case 4" at an angle of attack of 0°
and $U = 9\,\mathrm{m/s}$

Figure 4.23: Out of plane flow visualized with $\frac{\partial w}{\partial z}$ for "Case 1" at an angle of attack of 0°
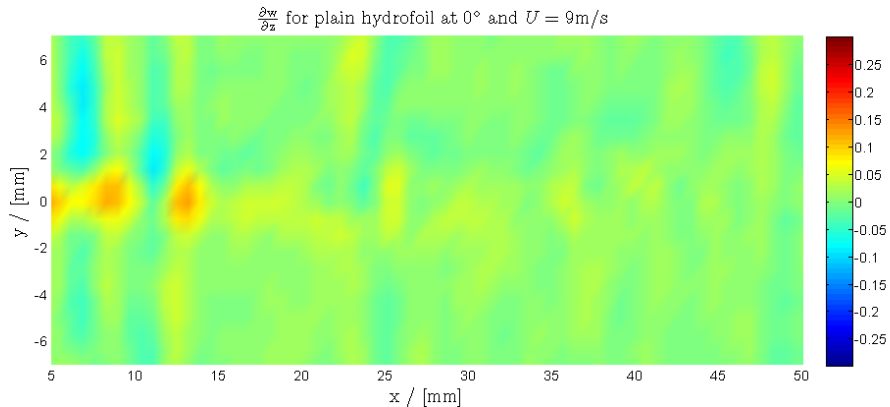and $U = 9\,\mathrm{m/s}$

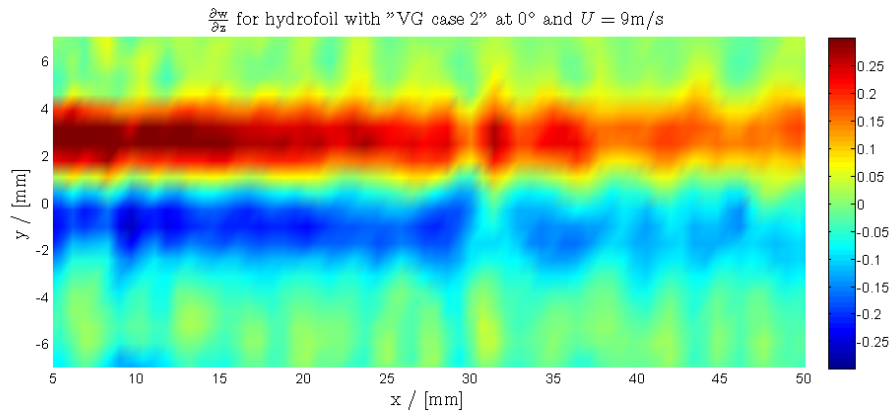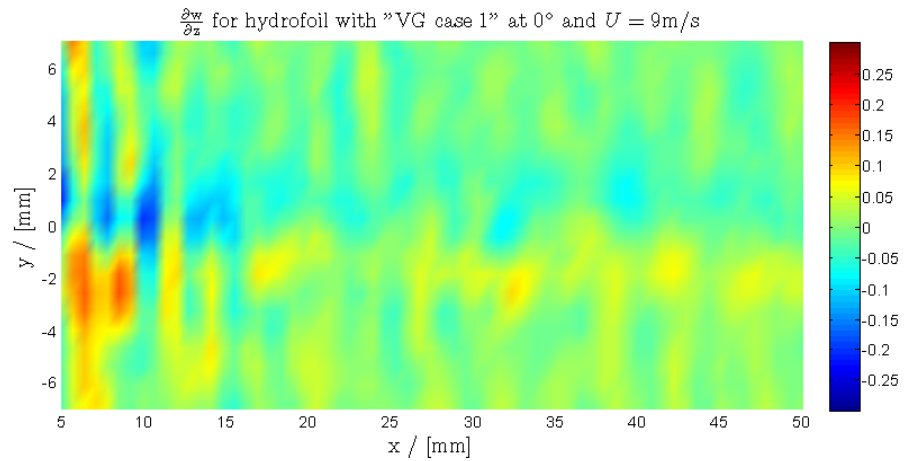
Figure 4.24: Out of plane flow visualized with $\frac{\partial w}{\partial z}$ for "Case 3" at an angle of attack of 0°
and $U = 9\,\mathrm{m/s}$
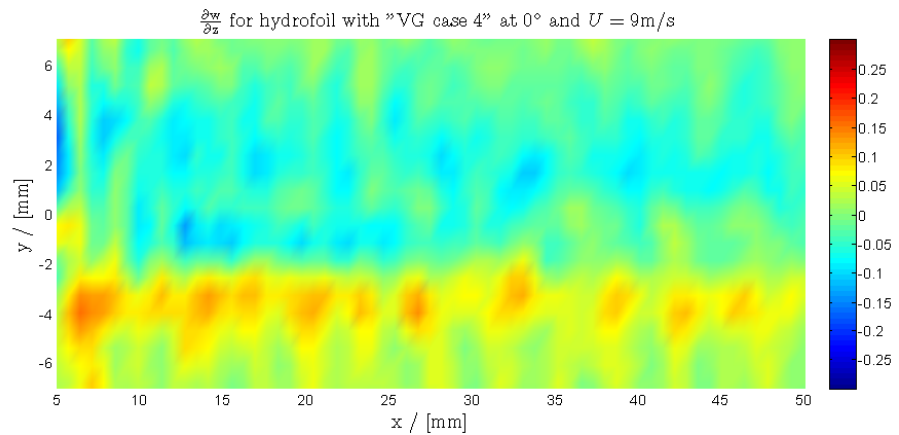
4.5.3   Height of Vortex Generators

A difference between the operation of the V-shaped vortex generators was observed. Thus
is was of interest to investigate how much the different VGs were penetrating the boundary

layer. To calculate the height of the boundary layer at a specific location on the hydrofoil, one can use software such as XFOIL to calculate the displacement thickness, see Figure 4.25.
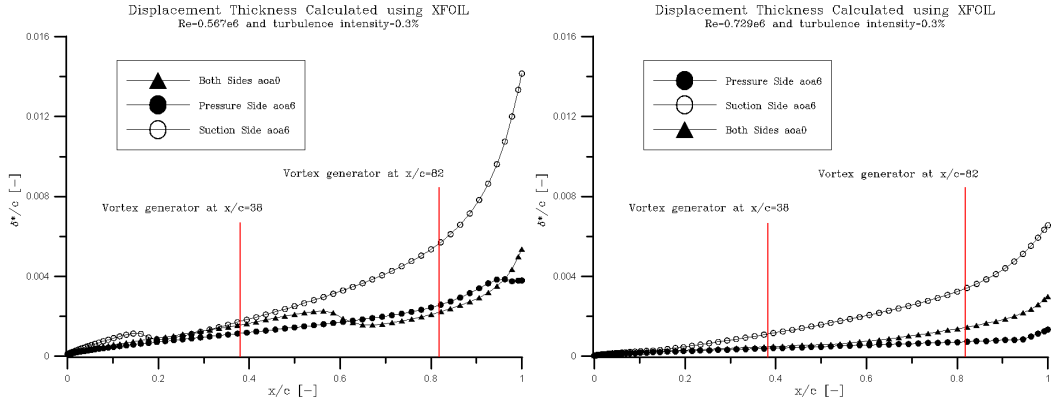

Figure 4.25: Displacement Thickness on a NACA0015 foil in $u = 7\,\mathrm{m/s}$ and $u = 9\,\mathrm{m/s}$ calculated with XFOIL

Note that we in XFOIL have to set the turbulent intensity to 0.3%, as it has been found to be in the SAFL water tunnel [20]. When the displacement thickness is found we can find the height of the boundary layer by using Prantl's estimate for turbulent flat-plate velocity profile expressed with displacement thickness (see Equation 4.1) [18, chapter 7.4]:

$$\delta \approx 8\delta^* \tag{4.1}$$

The insets for the vortex generators is at $x/c = 0.38$ and $x/c = 0.82$ from the leading edge. The calculated boundary layer thicknesses at the positions of the vortex generators are shown in Table 4.1

	Bottom surface, VGs at $x/c = 0.38$	Top surface, VGs at $x/c = 0.82$
$u = 7\,\mathrm{m/s},\ aoa = 0°$	1.0 mm	1.4 mm
$u = 7\,\mathrm{m/s},\ aoa = 6°$	1.1 mm	1.7 mm
$u = 9\,\mathrm{m/s},\ aoa = 0°$	0.9 mm	1.4 mm
$u = 9\,\mathrm{m/s},\ aoa = 6°$	1.1 mm	1.4 mm

Table 4.1: Boundary Layer Thickness

The V-shaped vortex generators were at the bottom surface of the hydrofoil. Note that the bottom surface will be the suction side for positive angles of attack in the way angles of attack have been defined in this report. In this way these VGs would be on the suction side for an angle of attack of 6°. We see that the 1 mm VG will be more inside the boundary layer at an angle of attack of 6° than 0°, hence we could expect a larger effect on the wake at 0°. On the same time higher velocity would decrease the boundary layer thickness and hence increase the effect of the vortex generator. This was confirmed when looking at the out of-plane-flow in terms of $\frac{\partial w}{\partial z}$ for VG case 2 at different velocities, see Figure 4.26. In this figure $\frac{\partial w}{\partial z}$ has got a higher absolute values for the 9 m/s case.

4.5.4 Turbulent Kinetic Energy

Another way to compare the operation of the different vortex generators is to look at the turbulent kinetic energy, see Section 2.4.4. The turbulent kinetic energy was calculated
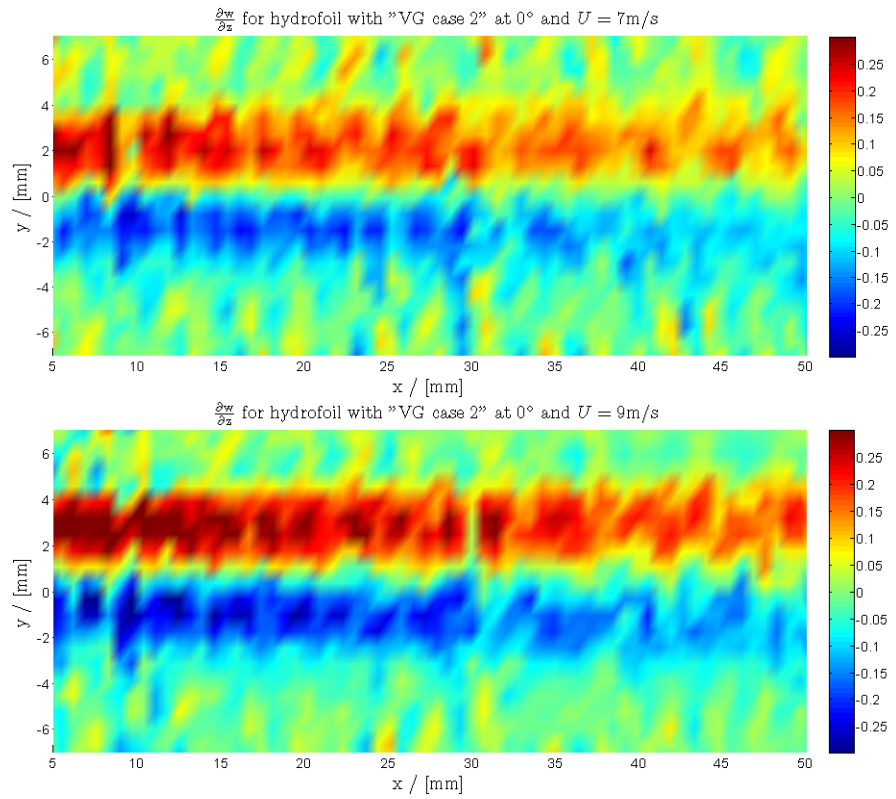
Figure 4.26: Out of plane flow visualized with $\frac{\partial w}{\partial z}$ for "Case 2" at $U = 9\,\text{m/s}$ and $u = 7\,\text{m/s}$

using DaVis7. The result was exported to Matlab for making the visualization better by using the same scales at all plots, see Figure 4.27, 4.29 and 4.28.
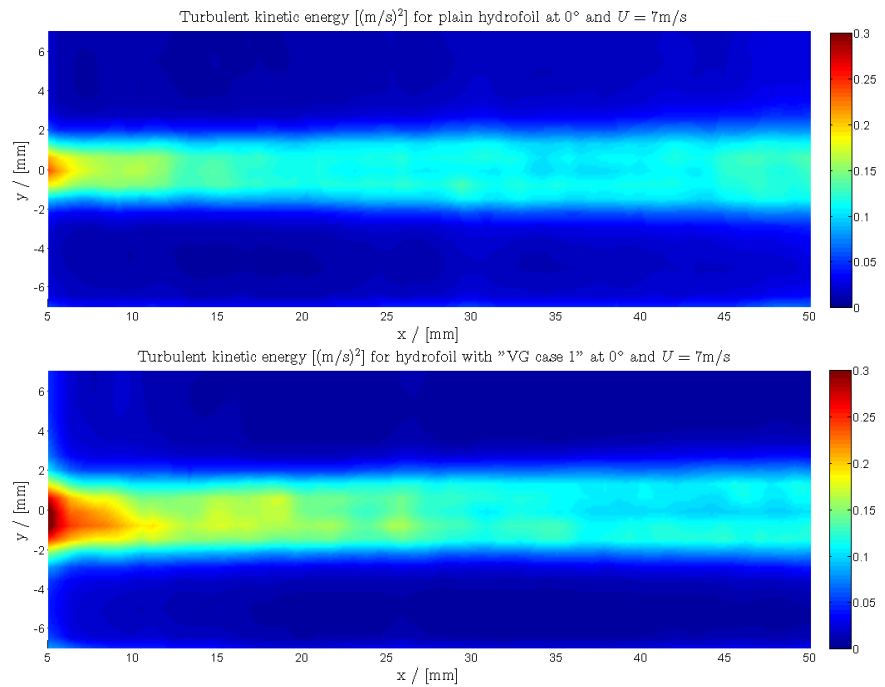
Figure 4.27: Turbulent kinetic energy in the wake of the plain hydrofoil and VG case 1
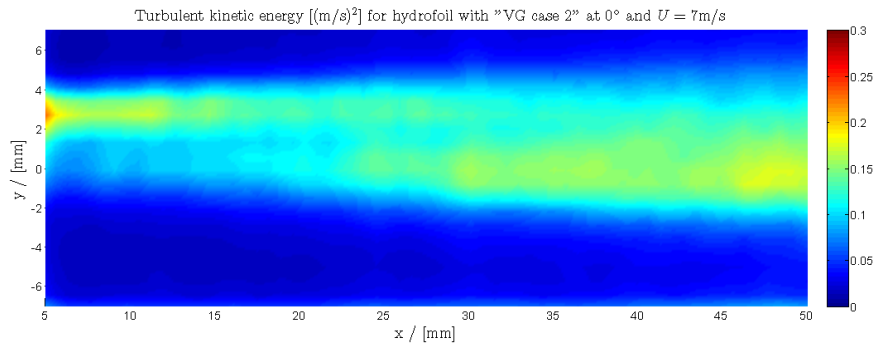
Figure 4.28: Turbulent kinetic energy in the wake of the hydrofoil with VG case 2

We can see that the turbulent kinetic energy is much lower for vortex generator case 2 than the rest of the tested cases. This makes the V-shaped 1 mm vortex generator very promising for smoothing out wakes for both turbulent velocity and the stationary velocity, as found in Section 4.5.1.
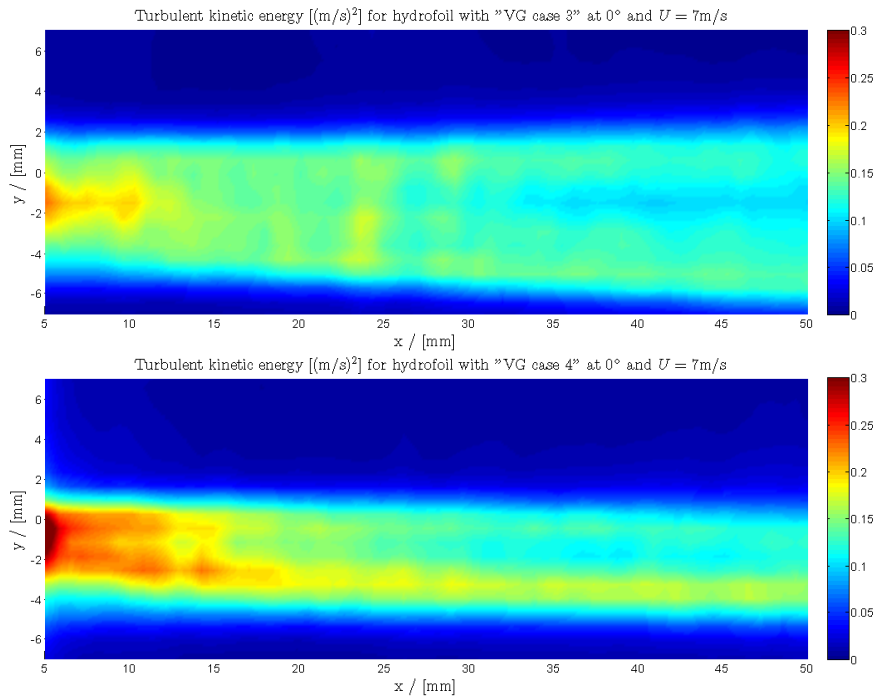
Figure 4.29: Turbulent kinetic energy in the wake of the hydrofoil with VG case 3 and 4

4.6   Energy Investigation

One of the things that could be interesting to investigate during this project was how the energy loss experienced as drag on the hydrofoil is transferred into the wake. The theory is that the energy must be conserved, hence the power used to hold a body in the stream must be found somewhere in the wake. Eventually the vortexes will get so small that the temperature in the flow will be increased, but close to the hydrofoil we can assume that most of the energy will be contained in the vortex structures in the wake. One expression for this Power balance have been suggested by Morten Kjelsen [7]:

$$DU \approx \bar{E} f_{shedding} \qquad (4.2)$$

where $\bar{E}$ is the average energy content in each vortex shed from the hydrofoil and $f_{shedding}$ is the shedding frequency of the vortexes from the hydrofoil. The drag and the velocity are the easiest ones to measure, I therefore wanted to investigate the shedding frequency and the energy content of the vortexes further. I have come up with some schemes that can be used for finding the shedding frequency. Unfortunately there was not enough time during this project to develop schemes for finding the energy content of the vortexes. However, as some work was done on this some suggestions for how to start this work is given in Chapter 6.

4.6.1   Frequency Investigation

To investigate the methods of finding frequencies tests were made on a cylinder of diameter $d = 12.7$ mm. As experimental results is easily accessible for cylinder vortex shedding it is easy to check that my frequency investigation techniques give reasonable results. This was also the reason for why tests were done on the cylinder.

The shedding frequency of vortexes from the trailing edge of the hydrofoil can be found in many different ways. One of the most robust ways is to use the PIV measurement to visualize the vortexes and then go through the recorded data and count the number of vortexes passing the field of view during the recording. The visualization was done by calculating the vorticity of the vector field. As described in Section 3.2 the interrogation area will be of great importance when making the visualization. But, even with a good visualization uncertainty is still involved in detecting the vortexes. If we estimate that there is a chance of missing one vortex out of 30 vortex pairs and the recording is lasting for typically 0.25 s there will be an uncertainty in the estimation of the frequency of ± 2 Hz.
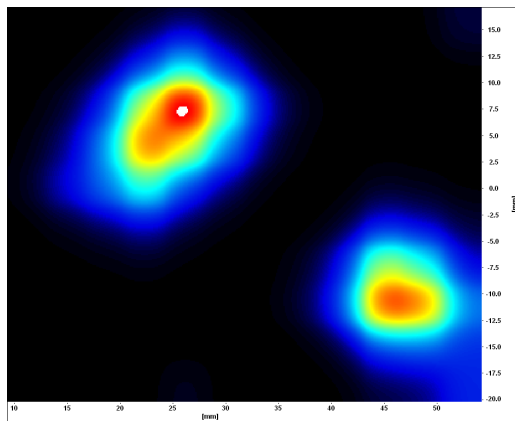

Figure 4.30: The visualization of vortexes by use of vorticity movies

Another way to investigate the shedding frequency is to use the recorded measurements of lift, drag or pressure and perform a Fast Fourier Transform (FFT) on the recorded data. This was possible to do only for the cylinder recording as the signals were not recorded continuously for the hydrofoil tests. When performing the FFT one had to be careful not to include outlier data in the analysis as this would distort the dominant frequencies. The recording for the cylinder at $3\,\mathrm{m/s}$ had a burst in the signal as that showed in Figure 4.33, and hence the FFT was done only on the validated part of the data. This analysis is showed in Figure 4.31. In this figure we see the grid frequency of $60\,\mathrm{Hz}$ showing up in the FFT analysis. The expected vortex shedding frequency for the cylinder in a flow of $3\,\mathrm{m/s}$ is $46\,\mathrm{Hz}$, using a Strouhal number of 21 [18, chapter 5.4]. The dominant frequency, other than the grid frequency, is found to by $42\,\mathrm{Hz}$, somewhat lower than the expected frequency.
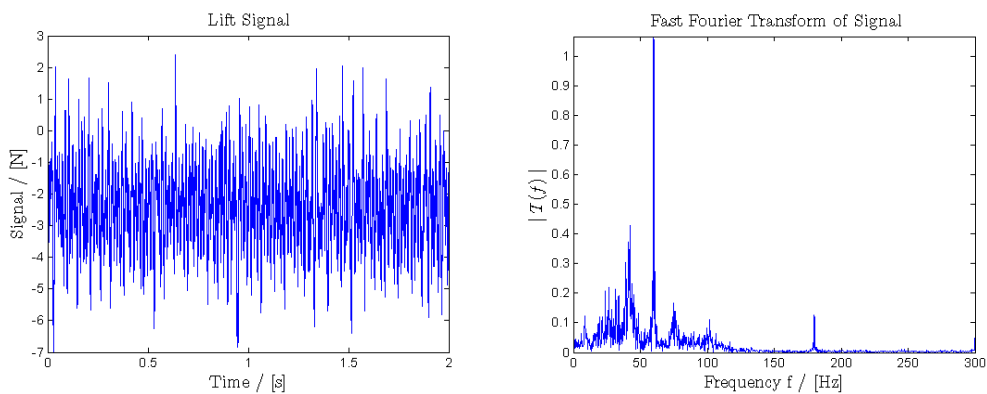
Figure 4.31: Lift Signal and corresponding FFT for cylinder case at 3m/s

An interesting observation could be made when the FFT-analysis was done on the drag measurement. The frequency being two times higher than the shedding frequency would show up in the drag measurement. The reason for this is that there is one pair of vortexes leaving the trailing edge during one shedding period. This is causing a pressure drop at the trailing edge two times each shedding period.

It is also possible to find the frequency of the vortex shedding by doing a FFT on the velocity field. In that case the frequency of change in velocity direction is studied. This can be performed using DaVis7. It did, however, appear to be difficult to obtain accurate results.

The different ways of finding the frequency shedding led to similar results. In figure 4.32 the results from the visual an FFT techniques have been compared. In general the frequency found by doing FFT on the lift measurement is a bit lower than the one found using visual inspection.
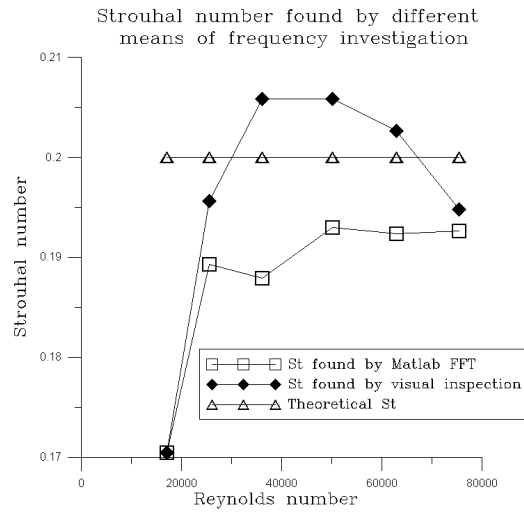
Figure 4.32: Strouhal number found by different means of frequency investigation techniques

4.7   Uncertainty

There have been different measurements done in this project. To validate the measurements an uncertainty analysis have been performed. Some of the uncertainties will be estimated using calculations from the the authors Fifth year project [15]. Good sources for quantifying measurement uncertainty are [17], [5] and [6].

4.7.1   Uncertainty in Force Balance

The force balance had problems with hystersis. This was taken care of in calibration by going to each calibration point from both less and more load. But still, both the lift and drag had offsets of the same order when starting and stopping measurements. The lift is many times larger than the drag for most angles of attack and hence the uncertainty is reduced.

When doing the hydrofoil measurements the signals were not recorded continuously, only the average values were stored for each test. For the test series with the cylinder, on the other hand, the signals were recorded continuously. When analyzing this data the signals seamed to be disturbed as illustrated in figure Figure 4.33. According to Morten Kjeldsen this is a problem they have had for a period of time, and being due to the frequency converter in the lab. When the cylinder measurements were analyzed it was found that the mean value of the signal was only affected minimally of such bursts.

Another aspect that was observed for the force balance was that there were an offset signal when the flow in the water tunnel had come to an stop. This is likely to be due to hysteresis in the force balance, which also was seen during calibration.

There has not been made an accurate analysis of the uncertainty of the force balance. This makes it nonviable to use the force balance to draw any accurate conclusions regarding the operation of the different vortex generators configurations tested.

4.7.2   Uncertainty in Pressure Measurement

The errors in the calibration of the pressure transducers can be combined by taking the root-sum-square (RSS) of the errors. One of the errors involved is due to the linear regression
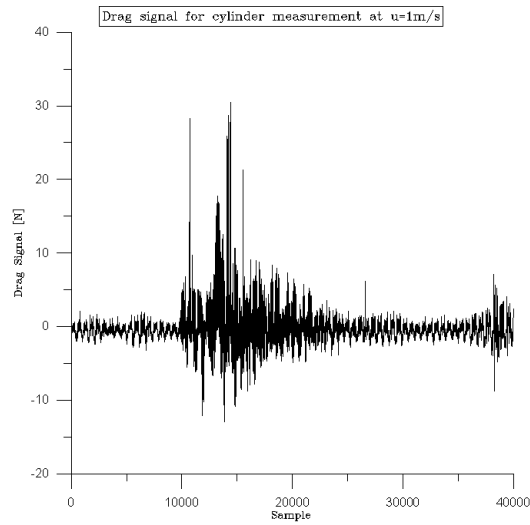
Figure 4.33: The recorded drag signal during the cylinder test.

of the calibration curve. A suggestion for the size of this error is given in the IEC standard [5]. Another error is associated with the spreading of the calibration points. By assuming this error to be about the same for this experiment as for the pressure calibration in [?], the total error in the calibration sum up to be about $f_{p,cal} = 0.07\%$.

During the test of the hydrofoil it was only the mean value of the the signal over 1 second that was recorded. It could be that there was a burst in the signal as shown in figure 4.33 during this recording. However, analysis of the data from the cylinder testes show that the mean values are not affected much by the bursts.

The differential pressure transducer is used to calculate the velocity in the tunnel. As the velocity is found with $U = \sqrt{\frac{2\Delta p}{\rho}}$, and the uncertainty in finding ρ can be ignored [15] the uncertainty in the calculated velocity is $f_u = 0.035\%$, which is ignorable.

At the end of the test a new calibration of the pressure transducers were performed confirming that the calibration that was used was still valid.

In conclusion the uncertainty in the pressure measurement can be ignored.

4.7.3 Uncertainty in PIV Measurement

I will only comment shortly on the largest sources of errors in PIV measurements. More information on errors in PIV measurements can be found in [21], [11] and [10].

The largest sources of errors in PIV measurements

Particle errors There will be an error in the measurement if the particles can not follow the flow. This error can be ignored as long as the settling velocity, the velocity the particle would sink or float up with, is much less than the velocity used in the test. If this settling velocity was 1 % of the velocity in the test, this error would be 1 %.

Magnification factor This will be due to calibration errors. As the calibration was done according to standards and the calibration was calculated with DaVis7 there is no reason to believe that there are any errors in the calibration.

Error in time between camera images The laser and camera is synchronized with the DaVis7 software. If the camera takes an image with a delay there will be an error in the

calculation of the velocity. There is however no reason to believe that there were any such errors in the PIV system.

Out-of-Plane Motion As the vortex generators will create out-of-plane flow there will be particles showing up in one interrogation area and not the next one in time, as particles will have moved out of the laser plane. This reduces the possibility for valid peak detection with cross-correlation. The peak detection will be good as long as a certain amount of particles are present in both frames.

Errors in Cross-Correlation This error will be affected by the size of the interrogation area and the type of cross correlation used. There is no straight forward way of calculating this error. Many things need to be done right in the processing of the vector field:

- there has to be enough particles in each interrogation area

- the particles can not move too far from one image to another

- the particles have to show up clearly in the image

- a suitable correlation scheme have to be used

If everything is done according to standards, this error can be ignored. If not, the calculated vector field may not represent the physical quantities tried measured. This is the most critical part of the PIV measurement and depend upon the user having sufficient knowledge about PIV measurement.

4.7.4   Uncertainty in PIV Post-Procesing

The results one get from post-processing of the vector field will depend greatly of the way the quantities are calculated. The vorticity for instance can be calculated using many different discretizations. The different discretizations will result in different values for the vorticity. No further effort has been done to quantify this error.

4.7.5   Uncertainty in CFD

A discussion of the main sources of error in CFD was given in Section 2.5.3.

Chapter 5

Conclusions

In this masters thesis different analysis schemes for PIV measurements have been investigated. Batch processing of PIV data and further post-processing have been carried out using the commercial PIV software DaVis7 and Matlab programs. The analysis scheme described in this report have shown to be robust for analyzing the PIV measurements obtained in this project.

A literature survey on wake flows have been carried out, with a summery given in this report.

The author have become familiar with existing PIV equipment and analysis through both, a literature survey on PIV and experimental work with PIV at Saint Anthony Falls Laboratory at the University of Minnesota. At SAFL, PIV measurements of the wake of a NACA0015 hydrofoil with different vortex generator configurations was carried out.

The results obtained during the experimental work have been discussed with the use of CFD.

As the project progress was good, the different wake manipulating techniques that were tested have been investigated. The amount of data to analyze only made it possible to look into measurements done with the hydrofoil at 0° and 6°.

From both PIV measurements and CFD simulation it was found that the "free stream" velocity outside of the wake is affected by the tests being performed in a water tunnel. The velocity in the wake will be lower than the almost uniform velocity upstream, this causes the velocity outside the wake downstream to be higher than upstream. The tunnel walls will also introduce shear stress on the water flowing in the tunnel. This friction will be experienced as a pressure drop in the tunnel. This pressure drop will come in addition to the pressure drop over the hydrofoil.

The force balance used to measure drag turned out to have too little accuracy to measure the drag difference between the vortex generator configuration. Consequently other ways to investigate this difference was investigated. In particular it was analyzed whether the velocity deficit in the wake can give information about the drag. Through the use of CFD is was seen that this $C_{D,imp}$ was related to C_D. Calculation of this velocity drag $C_{D,imp}$ indicates that the plain hydrofoil had the lowest drag for all the investigated tests and that VG case 1 had the lowest drag of the vortex generator configurations. This was surprising as this vortex generator was the highest of the V-shaped vortex generators.

The lift was also measured with the force balance. It is believed that both the lift and the drag measurement was affected by hysteresis in the force balance, but as the order of the lift force is much larger than the drag force the lift measurement will have less uncertainty than the drag measurement for operation points with an angles of attack. From the lift measurement it was observed that the use of vortex generators did change the lift of the

hydrofoil on the investigated operation points slightly.

The idea of using a standard wake profile to describe the wakes from the different vortex generator configurations have been investigated. It turned out that the wakes of the hydrofoil for many VG configurations were non-symmetrical. It might be that the wake will fit the standard wake profile further downstream, in which case the standard wake profile will still be a way to analyze differences in the operation of vortex generators.

The velocity in which the vortex generator is operating will affect the operation of the vortex generator by changing the boundary layer thickness. It was observed that the operation of the vortex generators was changed with velocity

When the frequency of the vortex shedding is to found the most accurate way of doing this is by counting the number of vortex passing by for an as long period as possible. However a more automatic and quite accurate alternative is to do a frequency analysis of the measured lift or drag, assuming a force balance able to capture the frequencies involved.

For the operation points that have been analyzed it can be concluded that the use of a 1 mm V-shaped vortex generator performed better than any of the other vortex generators tested when it came to smoothing of the wake. This VG configuration also appeared to have less drag than the other vortex generator configurations tested.

These findings support the use of turbulence generators for the use of wake manipulation. Whether vortex generators can be viable in industrial applications will have to be studied in more detail.

Chapter 6

Suggestions for Further Work

As the duration of this project have been limited not all the wanted analysis could be carried out. In this chapter some suggestions will be made for what aspects that could be looked into in the future.

6.1 Finish Analysis of Measured Data

As there was not enough time during this project to analyze all the PIV data. It would be very interesting to see how the vortex generator cases perform at other angles of attack. It is therefore suggested to continue the work on wake manipulation by analyzing the experimental results from this project.

It should be developed ways to compare many different operation points in terms of:

Mixing of the Wake   It is possible to pursue the use of the standard wake profile further. Even though the standard wakes profiles does not fit the wakes perfectly, it does give an idea of the maximum velocity deficit and the width of the wake.

On the other hand the maximum velocity deficit and the width of the wake can be good candidates for describing the different wakes. If the measurements are of high quality these parameters will more easily give relevant information about the wake.

Drag   Taking into account the quality of the drag measurement, it is suggested to compare the calculated drag from the velocity deficit in the wake, $C_{D,imp}$, for different operation points. out-of-plane flow.

Another aspect that would be interesting to look into is how the out-of-plane flow compare at different angles of attack for the different vortex generators.

6.2 Mean Energy Investigation

The power balance discussed in Section 4.6 could not be investigated further. It would be fulfilling to get the power balance right. One important step in this work would be to find the mean energy content of the vortexes in the wake. As the work was initialized during this project, a recapitulation of what has been done so far is give:

Morten Kjeldsen [**?**] have tried to estimate the energy content by modeling $\bar{E}$ as

$$\bar{E} = \frac{\pi}{4}\omega^2 a^4 \tag{6.1}$$

where a is the distance between the vortex pairs and ω represent the rotational speed of the vortex modeled as a flat plate with radius a. This will apparently facilitate the estimation of the energy content of the vortex but it is somehow difficult to find the rotational speed representing the vortex as a disc with a radius a.

The energy content of vortexes have also been investigated by Agrawal and Prasad in *Measurements Within Vortex Cores in a Turbulent Jet* [3] and *Properties of vortices in the self-similar turbulent jet* [2]. They found the energy content of different vortexes through the circulation around a vortex. But through this procedure one will have difficulties defining the path of integration, the radius of the vortex, for the circulation.

6.2.1   Radius Investigation

An easy way to investigate the radius of the vortexes is to use the vorticity fields calculated from the PIV results to visually look at the vortexes and estimate and average radius.

If a more refined method is required one can detect the vortexes and calculate the radius with a computer algorithm. This was done by Agrawal and Prasad in [**?**] and [2]. They filter the vector field with something they call a high pass filter, which appear to remove average velocities and make it easier to find vortexes. The non-linear filter "Large Eddie Simulation (LES) decomposition" algorithm in DaVis7 is believed to perform a similar filtering. The radius of the vortexes can then be found by analyzing the filtered vector field and looking for the largest closed path that can be made around the vortex centers with the vectors displaying a monotonic variation from 0 to 2π. It was shown that the vortexes could be simulated well as Rankine vortexes with radius as found over.

6.2.2   Angular velocity

The angular velocity can be calculated from the vector field found by PIV post-processing through the vorticity field. When the position of the vortex is found as described over one have to calculate the average angular velocity of that vortex.

Bibliography

[1] Ira H. Abbott and Albert E. von Doenhoff. *Theory Of Wing Sections, including a summery of airfoil data*. Dover Publications, Inc, 1959.

[2] Amit Agrawal and Ajay K. Prasad. Properties of vortices in the self-similar turbulent jet. *Experiments in Fluids*, 33:565–577, 2002.

[3] Amit Agrawal and Ajay K. Prasad. Measurements within vortex cores in a turbulent jet. *Journal of Fluids Engineering*, 125:561–568, May 2003.

[4] ANSYS. *Fluent Help Pages*.

[5] International Electrotechnical Commission. *IEC 60193: Hydraulic turbines - Model acceptance tests*, 1999.

[6] ISO. *Guide to the Expression of Uncertainty in Measurement*. International Standards Organization, 1993.

[7] Morten Kjeldsen. Experimental investigation of wake characteristics of modified hydrofoil shapes. Technical report, Flow Design Bureau AS, 2003. contact: morten.kjeldsen@ntnu.no.

[8] James E. Kopriva. Experimental study of a high performance partial cavitating hydrofoil under steady and periodic flows. Master's thesis, University of Minnesota, 2006.

[9] Arnol M. Kuethe. Control of noise and instablilities in jet engines, compressors, turbines, heat echangers and the like, Dec. 4 1973. US Patent no. 3776363.

[10] LA Vision. *DaVis 7 Help Pages*.

[11] S.Wereley J.Kompenhans M.Raffel, C.Willert. *Particle Image Velocimetry, A Practical Guide*. Springer, 2nd edition, 2007.

[12] J. Kompenhans M.Stanislas and J. Westerweel (Eds.). *Particle Image Velcimetry, Progress towards Industrial Application*. Kluwer Academic Publishers, 19–.

[13] H. Schlichting and K. Gersten. *Boundary Layer Theory*. Springer, 8th edition, 2000.

[14] Jeff Scott. Wing vortex devices. `http://www.aerospaceweb.org/question/aerodynamics/q0228.shtml`, 2005.

[15] Bjarte Grytli Seim. Flow conditions in a pelton runner. Technical report, NTNU, 2008. contact: bjartgr@stud.ntnu.no.

[16] H K Versteeg and W Malalasekera. *An Introduction to Computational Fluid Dynamics, The Finite Volume Method*. Pearson Prentice Hall, 2nd edition, 2007.

[17] Anthony J. Wheeler and Ahmad R. Ganji. *Introduction to Engineering Experimentation, Second Edition*. Pearson Prentice Hall, 2004.

[18] Frank M. White. *Fluiud Mechanics*. Springer, 8th edition, 2000.

[19] Frank M. White. *Viscous Flow*. Springer, 8th edition, 2000.

[20] Martin Wosnik. Description of safl high speed water tunnel and experimental equipment. `http://cav.safl.umn.edu/facilities.htm`, 2005.

[21] Martin Wosnik. Particle image velocimetry "a micro-course in macro-piv", 2007. Presentation from course given at UMN.

[22] Øyvind Antonsen. *Unsteady flow in wicket gate and runner with focus on static and dynamic load on runner*. PhD thesis, Norwegian University of Science and Technology, 2007.